Chemomechanics of Transfer Printing of Thin Films in a Liquid Environment

Yue Zhang [a #], Bongjoong Kim [b #], Yuan Gao [a], Dae Seung Wie [b], Chi Hwan Lee [b*], Baoxing Xu [a*]

[a] Department of Mechanical and Aerospace Engineering, University of Virginia, Charlottesville, VA, USA

[b] School of Mechanical Engineering, School of Electrical and Computer Engineering, Weldon School of Biomedical Engineering, Center for Implantable Devices, Purdue University, West Lafayette, IN, USA.

# These authors contribute equally

* Corresponding authors: lee2270@purdue.edu (CL), and bx4c@virginia.edu (BX)

Abstract

The liquid-assisted transfer printing is emerging as a competitive manufacturing technique in the delivery and assembly of thin film-layered functional materials and structures. In essence, this technique is underpinned by the detachment of thin films under a synergistic effect of external mechanical loading and interior chemical reaction at interfaces in a liquid environment. Here, we have developed a comprehensive chemomechanics theory for the transfer printing of thin films from as-fabricated SiO_2/Si wafer substrate in a liquid water environment. The kinetic chemical reaction at the interface of liquid molecules and interfacial solid bonds is incorporated into the interface energy release rate of thin film detachment, and a rate dependent interfacial debonding process is obtained. We further couple it with mechanical deformation of thin films by taking into account various peeling conditions including peeling rate, peeling angle and thin film thickness to theoretically predicate the steady-state peeling force. Besides, we implement this chemomechanics theory into a finite element model with all atomic information informed and present a reactive atomistic-continuum multiscale model to simulate the detachment of thin films at the continuum scale. In parallel, we have conducted the peeling experiments of three different separation layers on wafer substrates in both dry air and water conditions. Quantitative comparisons among theoretical predictions, simulation results, and experimental measurements are performed and good agreement is obtained. The competition between interfacial delamination and mechanical deformation of thin films during peeling is also analyzed, and a theoretical phase diagram is given to provide an immediate guidance for transfer printing of silicon nanomembranes in the fabrication of functional structures and electronic devices. In addition, the capillary force due to surface wettability of materials is discussed and compared with chemical reaction-induced driving force for transfer printing on a wide range of thin film/substrate systems. The chemomechanics theory and reactive atomistic-continuum simulation model established are expected to lay a foundation for quantitative understanding and descriptions of transfer printing of thin films in a liquid environment.

Keywords: separation layer; transfer printing; liquid environment; chemomechanics; reactive atomistic-continuum simulation modeling

1. Introduction

Transfer printing is a technique of assembling layered structures and devices down to the nanoscale by picking up a thin film processed on a donor substrate prior and releasing it onto a target receiver substrate, usually with the help of a soft stamp. The emergence of this manufacturing technique creates a wide range of application opportunities through its ability to separate requirements associated with donor and receiver substrates and to enable heterogeneous integration of dissimilar materials into well-organized layered functional structures (Carlson et al., 2012), in particular, in the fabrication of large-area, flexible and thin film electronic devices (Fan et al., 2008; Jung et al., 2010; Nam et al., 2009; Yoon et al., 2015).

Conventional transfer printing processes that control the spalling and enable the physical separation of material or device layers from their as-grown/deposited donor substrate rely strongly on an externally applied mechanical loading condition. For example, the kinetically-controlled transfer printing is used to deliver the thin films (Chen et al., 2013; Meitl et al., 2005). The success of this loading condition is closely associated with the retracting speed of the soft stamp at contact and depends on its viscoelasticity. Similar to this controlling mechanism, the shear loading that can control the initiation of cracks at the edges of contact area is also utilized in transfer printing, referred to as the shear-enhanced transfer printing (Carlson et al., 2011; Cheng et al., 2012). During these transfer printing processes, a large mechanical force is often required to physically separate the adhesive systems, and it may lead to unrecoverable and/or potential damage to functional thin films, in particular, fragile thin films. To improve the yield of transfer printing, several environmentally assisted methods have been proposed such as thermal-assisted mechanical peeling (Xu et al., 2016), the lifting-off or undercutting by chemical etching (Mahenderkar et al., 2017), electrochemical delamination (Bae et al., 2010; Li et al., 2009; Regan et al., 2010), and ultrasonication-induced microbubbles (Ma et al., 2015). For example, chemical-etching-assisted transfer printing, commonly referred to wet etching, has been developed (Yoon et al., 2010). Its working mechanism is to physically release thin films by chemically etching a thin interfacial sacrificial layer and thus reducing the interfacial adhesion. This chemical etching approach has been widely used for deterministic assembly of multilayered structures and large-area flexible electronics (Hwang et al., 2014). In

particular, it proves to be powerful in the transfer printing of graphene-grown on metal substrates (e.g. Fe, Ni, and Cu), where the entire seed metal needs to be completely etched away (Bae et al., 2010; Li et al., 2009; Regan et al., 2010). However, this chemical etching process requires a long period immersion of the entire devices in the etchant solution, especially for transfer of large-scale thin films, which is a great challenge for the embedded electronic components that need to be properly protected from degradation or/and damage (Pirkle et al., 2011; Suk et al., 2011) and contaminations (Mahenderkar et al., 2017). Besides, the chemical-etching cannot be well controlled and heavily relies on trial-and-error methods with a low yield in practice, and either the over-etching that will lead to floating of thin films (sometimes accompanied with subsequent collapse) or under-etching that will require a large mechanical force is considered the fail of transfer printing process. More importantly, the uses of chemicals such as hydrogen fluoride (HF), hydrochloric acid (HCI), and nitric acid (HNO_3) which are very harmful to human health and environments require to be operated in a great care with strict safety trainings in advance. In addition, the fabrication wafer is often consumed and cannot be recycled. Recently, we have demonstrated a proof of concept of water-assisted transfer printing process and it involves a very simple mechanical peeling of a metallic separation layer (i.e., Ni) in a water environment (Wie et al., 2018). Our demonstration shows that the thin-film nanoelectronics could be easily peeled off from the fabrication SiO_2/Si wafer in a defect-free manner. Similar technique has been used to create a wafer-size flexible devices by peeling single-crystal gold from SiO_2/Si substrate in a liquid environment (Mahenderkar et al., 2017). Because only liquid water is needed, this transfer printing is considered to be green and will have a significant impact in manufacturing.

In fundamental science, transfer printing is a peeling process with competing crack paths along the interface between either stamp and film or film and substrate. Several peeling and adhesion models have been developed over the past decades by considering elasticity of films (Peng and Chen, 2015), viscoelastic materials (Afferrante and Carbone, 2016; Peng et al., 2014), interfacial friction/sliding (Begley et al., 2013; Yao et al., 2008), heterogeneous structures (Xia et al., 2013) and micro-adhesive structures (Qian et al., 2017), and are expected to provide a quantitative guidance for applications to transfer printing in dry conditions (Chen et al., 2013;

Xue et al., 2015). However, for the transfer printing in a liquid environment, the detachment of thin films involves a synergistic effect of external mechanical loading and interior chemical reaction at the interfaces, and most of the existing chemomechanics work that is primarily focused on the crack growth in bulk materials, such as the li-ion battery and glass materials, is limited for this application purpose. For example, in the study of li-ion battery, the coupling of diffusion field of chemical species with mechanical field inside elastic solids is emphasized to obtain a modified J-integral and energy release rate (Gao and Zhou, 2013; Xu and Zhao, 2018; Zhang et al., 2017a). In the study of glass materials, the kinetics of silica dissolution is investigated to derive the crack growth velocity in the bulk glass (Vlassak et al., 2005). In particular, these coupling strategies cannot be applied to our proposed new concept of liquid-assisted transfer printing of thin films (Wie et al., 2018), where the hypothesis is that chemical reaction mainly occurs at the interface between liquid molecules and interfacial solid bonds and there is no chemical diffusion and reaction inside solid materials of both film and substrate. In addition, although there are a few works concerning the environment-assisted thin film debonding at the interface, they focused on either computational or experimental study, for example, DFT calculations in the investigation of moisture-induced interface fracture(Vijayashankar et al., 2011), and experimental characterization on the dependence of interface debonding rate on moisture(Kook and Dauskardt, 2002), and the underlying fundamental mechanics theory is lacking. Therefore, a comprehensive theoretical model that could couple the kinetic chemical reaction at interfaces and mechanical deformation of thin films is highly needed.

In the present study, we establish a comprehensive chemomechanics theory of functional thin film detachment from the most popular ceramic/dielectric donor substrate (e.g. silicon on insulator (SOI) wafer) in a liquid water environment with the help of separation layer. We also develop an atomistic-continuum computational model by implementing the information completely informed from atomistic reactive simulations into finite element model for predicting macro-fracturing phenomena parallel with experimental validations. The details of theoretical development of chemomechanics theory are presented in Section 2. Kinetic chemical reaction theory is proposed to obtain the rate dependent interfacial energy release rate

and is also incorporated into the interface fracture process of thin film and substrate. The mechanical deformation of thin film is described by the elastic-plastic model and coupled with the chemical reaction-controlled interface fracture to predict the peeling force at the steady-state peeling process. In Section 3, an atomistic-continuum modeling framework is developed and implemented into the finite element model to simulate and predict the entire liquid-assisted peeling process. Reactive molecular dynamics (MD) simulations are first performed to extract atomistic chemical reaction associated with interfacial debonding and validate the theoretical model. These MD information is then implemented into finite element (FE) model via interfacial cohesive zone model (CZM) to establish an atomistic-continuum computational model to address the macro-fracturing process of interface in the transfer printing. Experimental setups and procedures are also presented in Section 3. Theoretical predictions, simulation analyses, and experimental results are discussed and compared in Section 4. In Section 5, the practical application of theoretical models to transfer printing of silicon nanomembranes is analyzed by taking into account the competition between the deformation-induced failure strain of functional thin films and the interfacial delamination. Phase diagrams toward the successful transfer printing are given and compared with those in dry air conditions. Extended discussion on the effect of surface wettability on interfacial delamination and its competition with chemical reaction-induced driving force for applications in different film/substrate systems are discussed in Section 6. Concluding remarks are given in Section 7.

2. Chemomechaics model development

In essence, the transfer printing process can be simplified to a peeling mechanics model. **Figure 1 (a)** illustrates the concept of peeling a functional thin film grown or processed on a substrate in a liquid environment. During the peeling process, the interfacial fracture initiates and propagates between the separation layer and substrate under the combined efforts of the applied peeling load and chemical reaction, and in the following analysis, only the separation layer on substrate will be considered, otherwise stated. In the chemical reaction theory, the liquid environmentally assisted interface fracture can be considered a stress enhanced chemical reaction between highly strained interfacial bonding at the interface fracture tip and reactive

species in the environment, as shown in the right schematic of atomistic illustration in Figure 1 (a). During the peeling process, the applied mechanical loading will stretch the interfacial bonds near the debond-tip, and the adsorption of liquid molecules will weaken these interfacial bonds. The combined action of applied load and corrosive effect of chemisorbed species causes these bonds to rupture at a certain rate, which leads to the interface crack propagation (Kook and Dauskardt, 2002; Vlassak et al., 2005).

Consider the interfacial fracture process as a sequence of atomistic bond ruptures associated with the general chemical reaction via

$$A + nX \leftrightarrow C \leftrightarrow B \tag{1}$$

where A represents an unbroken interfacial bond, X is the reactive liquid molecules from the liquid environment, C represents the activated transition complex and B represents the final reaction products, i.e., the resultant broken bonds terminated with the appropriate functional groups. The change of Gibbs free energy associated with the forward reaction in Equation (1) per unit of crack area is

$$G_0 = (\mu_B - \mu_A - n\mu_X)N \tag{2}$$

where μ is the chemical potential of reactants and reaction products of A, X, and B, and N is the number of interfacial bonds per unit area. Because the forward chemical reaction in Equation (1) leads to the creation of a new surface, we have

$$G_0 = \gamma \tag{3}$$

where γ is the total surface energy per unit area from the new fractured surface. In general, the creation of this new surface area requires an external energy, and thus γ is positive, suggesting a higher energy associated with the reaction products than that of the reactants. The chemical reaction in Equation (1) is a dynamic and reversible process. The forward reaction leads to bond breaking and is responsible for the crack growth; the reverse reaction leads to bond formation and is responsible for the crack healing. The interfacial crack propagation velocity can be determined by such the forward and reverse kinetics of the chemical reaction at the crack tip (Cook and Liniger, 1993; Lawn, 1975; Wiederhorn et al., 1980). Consider the bond rupture governed by Maxwell-Boltzmann statistics (Lawn, 1975), the rate of bond breaking can be determined by

$$\vec{\omega} = \frac{kT}{h}\exp(-\frac{\vec{E}_0{}^*}{kT}) \tag{4}$$

where $\vec{E}_0{}^*$ is the activation energy for bond breaking, k is Boltzmann's constant, T is the absolute temperature, and h is Planck's constant. Similarly, the rate of bonding healing in the reverse reaction can be written as

$$\overleftarrow{\omega} = \frac{kT}{h}\exp\left(-\frac{\overleftarrow{E}_0{}^*}{kT}\right) = \frac{kT}{h}\exp\left(-\frac{\vec{E}_0{}^* - \gamma/N}{kT}\right) \tag{5}$$

where $\overleftarrow{E}_0{}^*$ is the activation energy for bond healing. Therefore, the net rate of the kinetic chemical reaction is

$$\omega = \vec{\omega} - \overleftarrow{\omega} = \frac{kT}{h}[\exp(-\frac{\vec{E}_0{}^*}{kT}) - \exp\left(-\frac{\vec{E}_0{}^* - \frac{\gamma}{N}}{kT}\right)] \tag{6}$$

When there is no external applied mechanical loading, the energy barrier of the reverse reaction is lower than that of the forward reaction, and the rate of the reverse reaction is higher than the forward reaction. As a consequence, the net chemical reaction would lead to the crack healing, rather than crack growth. In contrast, when an external mechanical load is applied, the interfacial bonding is being stretched, and the resultant energy release rate, G, provides a driving force for the occurrence of forward reaction meanwhile suppressing the reverse reaction. Based on Lawn's kink model (Lawn, 1975), the imposition of the mechanical energy release rate will lead to changes of the energy barriers to bond rupture and healing, and the activation energy for bond breaking is

$$\vec{E}^* = \vec{E}_0{}^* - \frac{G}{2N} \tag{7}$$

where G/N is the amount of mechanical energy available per bond. Similarly, the activation energy for bond healing is

$$\overleftarrow{E}^* = \overleftarrow{E}_0{}^* + \frac{G}{2N} \tag{8}$$

Therefore, when an external mechanical loading is applied, the net rate of the chemical reaction becomes

$$\omega = \frac{kT}{h}[\exp(-\frac{\vec{E}_0{}^* - \frac{G}{2N}}{kT}) - \exp\left(-\frac{\vec{E}_0{}^* - \frac{\gamma}{N} + \frac{G}{2N}}{kT}\right)] \tag{9}$$

Figure 1 (b) illustrates the variation of energy in both forward and reverse reactions. Specifically, when the mechanical energy release rate G is smaller than γ (i.e. G_0), the energy barrier of the forward reaction $\vec{E}^*$ is larger than that of the reverse reaction, $\overleftarrow{E}^*$, i.e. $\vec{E}^* > \overleftarrow{E}^*$ and the crack will not grow. In contrast, when G is larger than γ (i.e. G_0), we will have $\vec{E}^* < \overleftarrow{E}^*$, and the rate of the forward reaction is larger than that of the reverse reaction, leading to the propagation of interfacial crack. At $G = \gamma$ (i.e. G_0), we will have $\vec{E}^* = \overleftarrow{E}^*$, and both forward and reverse reactions occur with the same rate, which corresponds to a stationary interfacial crack and γ is considered the threshold of driving energy for the crack propagation. Therefore, the resultant crack growth rate v_c can be determined by

$$v_c = \frac{kTb}{h}\left[\exp\left(-\frac{\vec{E}_0{}^* - \frac{G}{2N}}{kT}\right) - \exp\left(-\frac{\vec{E}_0{}^* - \frac{\gamma}{N} + \frac{G}{2N}}{kT}\right)\right] = 2\frac{kTb}{h}\exp\left(-\frac{E_a{}^*}{kT}\right)\sinh\left(\frac{G-\gamma}{2NkT}\right) \quad (10)$$

where b is the interfacial bond length, and $E_a{}^* = \frac{\vec{E}_0{}^* + \overleftarrow{E}_0{}^*}{2}$. With Equation (10), the interfacial energy release rate can be written as

$$G(v_c) = G_0 + 2NkT\sinh^{-1}\left(\frac{v_c}{2(kT/h)be^{\left(-\frac{E_a{}^*}{kT}\right)}}\right) \quad (11)$$

In Equation (11), the first term represents the intrinsic interfacial energy between film and substrate and equals to the change of Gibbs free energy associated with the interface fracture. From Equation (2), apparently, the presence of liquid molecules that will chemically react with solid phase at the interface and will lead to a reduction of interfacial energy release rate, promoting the interfacial delamination. The second term describes the rate dependence of the interfacial adhesion energy G.

During the detachment of thin film, the applied peeling force will also mechanically deform the thin film, and the resultant mechanical energy will compete with interfacial crack growth. Consider the thin film with thickness t, it will experience elastic-plastic bending deformation under an external peeling strength P with a loading angle α (see Appendix A, Figure A1(a)). The peeling strength P is defined as the peeling force per unit width of film.

According to the balance of local force in the normal direction, the equilibrium equation of force can be written as

$$\frac{dT}{ds} - KV = 0 \tag{12}$$

where T is the tensile force per unit width along the film, V is the shear force normal to the film, and s is the arc length along the film. K indicates the local curvature and $K = d\theta/ds$, where θ is the tangential angle. In addition to the force balance equilibrium equation, we have a moment-balance equilibrium condition and it is

$$\frac{dM}{ds} + V = 0 \tag{13}$$

where M is the local bending moment per unit width. Equations (12) and (13) lead to

$$\frac{dT}{ds} + K\frac{dM}{ds} = 0 \tag{14}$$

that is,

$$T + KM - \int MdK = constant \tag{15}$$

Substituting the global force equilibrium equation $T = Pcos(\alpha - \theta)$ into Equation (15), we will have

$$Pcos(\alpha - \theta) + KM - \int MdK = constant \tag{16}$$

Because every point in the peeled film needs to satisfy this equilibrium condition, the bending moment-curvature relation for all sections of film can be derived (see Appendix A). Apply these relations into Equation (16), we will have the equilibrium equation of mechanical deformation for the entire thin film, and it is

$$P - Pcos(\alpha - \theta_B) + \frac{(K_{max}Et - 4\sigma_y)^2 Et}{24} - \frac{{K_{max}}^2 Et^3}{24} - \frac{\sigma_y K_{max} t^2}{6} + \frac{4{\sigma_y}^2 t}{3E} - \frac{8{\sigma_y}^3}{3E^2 K_{max}} = 0 \tag{17}$$

where K_{max} is the maximum curvature in the thin film and $\theta_B = \frac{2K_{max}E^2 t}{3{\sigma_y}^2}$ (Kinloch et al., 1994). And E and σ_y are the Young's modulus and yield stress of the thin film, respectively. Equation (17) gives the relation between the applied peeling strength and the maximum curvature in the thin film.

During the peeling process at the steady state, the energy conservation needs to be satisfied and the work done by the applied force (W_P) must balance the changes of the interface adhesion energy (W_{ad}) and the energy dissipated in the deformation of thin film (W_d), which is

$$W_P = W_{ad} + W_d \tag{18}$$

For the thin film to be peeled with an incremental length dl under the steady-state condition, the work done by the peeling strength is $W_P = P(1 - cos\alpha)bdl$ and the change of the interfacial adhesion energy is $W_{ad} = Gbdl$, where b is the width of thin film and G is the interfacial energy release rate that is given in Equation (11). The dissipation energy is associated with the plastic bending deformation of film, and is $W_d = Qbdl$, where Q is the plastic work per unit area. Consider the steady-state peeling process, the internal plastic work of the thin film can be obtained via $Q = \int_l M(K)dK$, and is assumed to be rate independent under low peeling rate (Kim and Aravas, 1988). With the bending moment-curvature relations for all sections of thin film (see Appendix A), the plastic work in the peeled thin films can be obtained as

$$Q = \frac{\sigma_y t^2 K_{max}}{2} - \frac{5\sigma_y{}^2 t}{2E} + \frac{10\sigma_y{}^3}{3E^2 K_{max}} \tag{19}$$

With these energy analysis, we will have

$$P(1 - cos\alpha) = G + Q \tag{20}$$

Substituting Equations (11) and (19) into Equation (20) will yield

$$P(1 - cos\alpha) = G_0 + 2NkTsinh^{-1}\left(\frac{v_p/(1\text{-cos}\alpha)}{2(kT/h)be^{\left(-\frac{E_a{}^*}{kT}\right)}}\right) + \frac{\sigma_y t^2 K_{max}}{2} - \frac{5\sigma_y{}^2 t}{2E} + \frac{10\sigma_y{}^3}{3E^2 K_{max}} \tag{21}$$

where v_p is the rate of peeling front propagation (i.e. velocity at the peeling front) and it can be correlated with the debonding tip propagation rate v_c (i.e. extension of interfacial crack per unit time) via $v_p = v_c(1 - cos\alpha)$ (Zhao and Wei, 2008). The K_{max} can be calculated by substituting the expression of P in Equation (21) to Equation (17). We should note that when the kinetic chemical reaction of liquid and interfacial solid bonds at interface is neglected, and the interface energy release rate remains a constant value G, the energy equation (21) will reduce to $P(1 - cos\alpha) = G + \frac{\sigma_y t^2 K_{max}}{2} - \frac{5\sigma_y{}^2 t}{2E} + \frac{10\sigma_y{}^3}{3E^2 K_{max}}$, which agrees with our previous work (Wie et al., 2018). And when the plastic deformation of the thin films is also neglected, the energy equation (21) will reduce to the classical Kendall model and $P(1 - cos\alpha) = G$(Kendall, 1975), where $G = G_0 + 2NkTsinh^{-1}\left(\frac{v_p/(1\text{-cos}\alpha)}{2(kT/h)be^{\left(-\frac{E_a{}^*}{kT}\right)}}\right)$.

Further combination of mechanical deformation via Equation (17) and energy conservation via Equation (21) will lead to

$$\overline{P}^2(\overline{\alpha}-1)(5\overline{\alpha}-4)-\overline{P}[3(5\overline{\alpha}-4)\overline{t}-(9\overline{\alpha}-8)\big(1+f(\overline{v})\big)-cos\alpha]+4\Big(3\overline{t}^2-3\overline{t}\big(1+f(\overline{v})\big)+\big(1+f(\overline{v})\big)^2\Big)=0 \tag{22}$$

where $\overline{P}=P/G_0$, $\overline{\alpha}=1-\cos(\alpha-\theta_B)$, $f(\overline{v})=\frac{2NkT}{G_0}sinh^{-1}\left(\frac{\overline{v}/(1\text{-}cos\alpha)}{2e^{\left(-\frac{E_a^*}{kT}\right)}}\right)$, $\overline{v}=v_p/(kTb/h)$ and $\overline{t}=t/(6EG_0/\sigma_y)$. With Equation (22), we can in theory predict the peeling strength P at the steady state by considering both chemical reaction and mechanical deformation-induced interfacial delamination.

3. Computations and experiments

3. 1 Reactive molecular dynamics simulations

Reactive molecular dynamics (MD) simulations were first performed to investigate the interface atomistic debonding and they also allow to determine the associated interface cohesive properties. To reproduce the atomic debonding and related chemical reactions, ReaxFF reactive force field was employed(Van Duin et al., 2001). This potential function could provide a reactive force field by using the bond-order term in conjunction with a charge equilibration scheme. The formation and dissociation of the atomic bonding could be recognized by atomic distances as well as the charge variations of the atoms. Our simulation modeling included two layers of materials, metal thin film with face-centered cubic (FCC) crystal structures in contact with a substrate. The most popular metal nickel (Ni) was studied as an example, and the substrate was taken as SiO_2 which is the top material layer of as-employed silicon-on-insulator (SOI) wafer in standard micro/nanofabrication. Their thicknesses were 4.5 nm and 5.2 nm, respectively. Simulations in both dry and liquid conditions were performed. In dry condition, the metal film layer and SiO_2 substrate layer were placed near each other in z-direction to generate an initial contact. To mimic the liquid water environment, the hydroxyl groups (OH) and hydrogen atoms (H) were added to the interface

between the Ni metal film and SiO_2 substrate (Lee et al., 2013). The most popular force field parameters were employed (Fogarty et al., 2010; Mueller et al., 2010; Van Duin et al., 2001). A periodic boundary condition was applied in in-plane (x-y) directions. All the simulations were carried out using the Large-scale Atomic/Molecular Massively Parallel Simulator (LAMMPS) package (Plimpton, 1995).

The reactive MD simulation procedure consisted of two steps: the system was first equilibrated in the isobaric-isothermal ensemble (NPT) for 25 ps with a constant temperature of 300 K and a pressure of 1 bar so as to achieve the initial physical state of the materials system. During the equilibration process, for the system in dry condition, the interfacial bond between surface nickel atoms in metal film and surface oxygen atoms in SiO_2 substrate was spontaneously formed; for the system in liquid water condition, the hydroxyl (OH) groups at the interface formed bond with the surface Ni atoms in the film and the hydrogen (H) atoms bonded with the surface oxygen (O) atoms in SiO_2 substrate, which agrees with both density functional theory calculations and reactive atomistic simulations (Lee et al., 2013; Vijayashankar et al., 2011). After the equilibration, a tensile load at a certain rate was applied to the z-direction in canonical ensemble (NVT) with Nose/Hoover thermostat at the temperature 300 K to study the interface debonding process, where the top boundary atoms of Ni layer were displaced upward along the z-direction during simulation, and the bottom boundary atoms of the SiO_2 substrate were fixed. At each displacement increment, the potential energy of the new molecular topology $E_{potential}$ was calculated (referred to the initial state). The interfacial stress was calculated via $\sigma = \frac{\Delta E_{potential}}{A\Delta d}$, where σ was the interfacial stress, A and Δd were the interfacial area and the variation of displacement, respectively. $\Delta E_{potential}$ corresponded the variation of system potential energy. The simulation step was set 0.25 fs so as to capture features of bonding formation and breaking and its dependent quantities.

Figure 2 (a) shows the curve of potential energy per unit area – displacement from MD debonding simulations. The system energy increases as the separation distance increases. When the metal and SiO_2 were completely separated, the system energy reached the maximum which is the interfacial adhesion energy G, and $G = 0.77 \text{J/m}^2$ and $G = 0.2$ J/m^2 at a quasi-static loading condition in dry and liquid water conditions, respectively. **Figure 2 (b)** plots the curve

of the interfacial stress-displacement. The interfacial stress first increases till to a peak value σ_p and then decreases with the increasing of the interfacial separation till to zero at the arrival of the complete separation of Ni film from the SiO_2 layer with a separation distance d_c. The peak interfacial stress $\sigma_p = 0.38$GPa and $\sigma_p = 0.13$GPa in dry and liquid water conditions, respectively. **Figure 2 (c)** gives the MD simulation snapshots of the debonding process in both dry and water conditions. At the dry condition, the debonding occurred at the interfacial bond between metal and SiO_2, yet with partial bond broken inside the metal near the interface, resulting in the metal residues of Ni atoms on SiO_2 surface, which agrees well with the experimental observations (Lee et al., 2013). In contrast, at the water condition, the debonding occurred at the interface without any atoms of metal residues on SiO_2 surface, indicating that the liquid-assisted transfer printing will help achieve a clear substrate for reuse.

When the metal/SiO_2 interfacial delamination occurs, from theoretical analysis in Section 2.1, the related bonding rupture process in Equation (1) becomes

$$\begin{cases} M - O - Si \leftrightarrow M + Si - O, & \text{in dry environment} \\ M - O - Si + H_2O \leftrightarrow M - OH + Si - OH, & \text{in water environment} \end{cases} \tag{23}$$

where the metal M is the Ni. As a consequence, the corresponding change of Gibbs free energy (equals to G_0) in Equation (2) is

$$\begin{cases} G_0 = (\mu_M + \mu_{Si-O} - \mu_{M-O})N\ , & \text{in dry environment} \\ G_0 = (\mu_{M-OH} + \mu_{Si-OH} - \mu_{M-O} - \mu_{H2O})N, & \text{in water environment} \end{cases} \tag{24}$$

where μ_M, μ_{Si-O} and μ_{M-O} are the chemical potential of the metal, the oxygen-terminated Si surface, and the metal-oxygen bond, respectively (Lane, 2003). μ_{M-OH} and μ_{Si-OH} are the chemical potential of the hydroxyl group-terminated metal and Si surfaces, respectively. Therefore, according to Equation (24), we can in theory obtain $G_0 = 0.74$J/m^2 in dry condition and $G_0 = 0.22$J/m^2 in liquid water condition, and they both agree well with the maximum interfacial adhesion energy G obtained from MD simulations at the quasi-static loadings (0.77J/m^2 and 0.2J/m^2, respectively) in Figure 2 (a), which validates reactive MD simulations. In addition, the good agreement of interfacial adhesion energy G between MD simulations and theoretical calculations indicates that the effect of bulk deformation on interfacial debonding can be neglected, which is also in consistency with residues of a few atoms in dry condition or clear interface in liquid condition in Figure 2(c). When the dynamic loading conditions change under different debonding rate v_c, similar simulations can also be conducted.

The results are given in appendix A, and the obtained interfacial adhesion energy G represents the coupling of loading rate with the intrinsic energy G_0 (quasi-static loadings), as shown in Equation (11).

3. 2. Computational implementation to finite element (FE) model for multiscale simulations

In the continuum scale, the cohesive zone model (CZM) is commonly used to model interfacial delamination and could also be integrated with atomistic information. In this section, we will implement the reactive MD simulations and theoretical results into CZM and establish an atomistic information informed-finite element modeling to study the peeling of thin film in a liquid environment (Kook and Dauskardt, 2002). **Figure 3 (a)** illustrates the cohesive zone at the fracture tip, where σ is the interface adhesive traction and δ is the interface separation. When the interface energy release rate reaches the critical energy release rate of interface, the interfacial traction drops to zero, leading to a complete separation. Γ_c is the critical energy release rate and can be determined by the area under the curve of traction-separation relation via

$$\Gamma_c = \int_0^{\delta_c} \sigma(\delta) d\delta = \sigma_0 \delta_c \int_0^1 \chi(\lambda) d\lambda \tag{25}$$

where σ_0 is the maximum interface cohesive strength, and δ_c is critical crack tip separation. $\chi(\lambda)$ specifies the shape of the traction–separation function with $\chi = \sigma/\sigma_0$ and $\lambda = \delta/\delta_c$. From the theoretical analysis in Section 2.1, Γ_c equals the interface debonding energy per unit area (G) in Equation (11) and can also be obtained from reactive MD simulations, and we have

$$\Gamma_c = G(v_c) = G_0 + 2NkT sinh^{-1}\left(\frac{v_c}{2(kT/h)be^{\left(-\frac{E_a^*}{kT}\right)}}\right) \tag{26}$$

With Equation (26), we can incorporate the effect of chemical reaction on the interfacial fracture by inputting $G(v_c)$ into CZM. Besides, this debonding energy varies with debonding rate v_c , and thus this obtained continuum CZM is a rate dependence. Therefore, once the interfacial adhesion energy and the maximum interfacial stress are obtained from reactive MD simulations in Section 3.1, they can be incorporated into CZM to study the interfacial delamination using finite element (FE) model. In addition, from analysis in Section 2.1, the

interfacial energy release rate is reduced in a liquid environment compared with that in dry condition, and a smaller interface fracture toughness in liquid condition ${\Gamma_c}^l$ than that in dry condition ${\Gamma_c}^d$ can be obtained, as illustrated in Figure 3 (a).

The curve of interfacial stress-displacement from reactive MD simulations in both dry and water conditions in Figure 2(b) shows that it can be fitted very well using a trapezium shape, as shown in Figure 3 (b). Besides, the trapezium shaped traction-separation law in CZM has been widely used to model the relation between δ and σ in elastic-plastic peeling problems (Tvergaard and Hutchinson, 1993). We should note that the interface fracture process by peeling a thin film is generally normal-separation dominant, and the mixed-mode effects can be neglected (Tvergaard and Hutchinson, 1993; Wei and Hutchinson, 1997). Moreover, the good agreement between MD simulations and theoretical calculation on the interfacial adhesion energy G further indicates that the shear effect can be neglected. Therefore, in the present study, the trapezium shaped traction-separation CZM will be used to corporate with atomistic information obtained from reactive MD simulations. As illustrated in Figure 3(b), $\chi(\lambda) = \frac{\lambda}{\lambda_1}$, at $0 < \lambda < \lambda_1$;$\chi(\lambda) = 1$, at $\lambda_1 < \lambda < \lambda_2$; and $\chi(\lambda) = -\frac{1}{1-\lambda_2}\lambda + \frac{1}{1-\lambda_2}$, at $\lambda_2 < \lambda < 1$, where λ_1 and λ_2 are the shape parameters. The fracture toughness in Equation (26) can be further rewritten as $\Gamma_c = \sigma_0\delta_c\int_0^1 \chi(\lambda)d\lambda = \frac{1}{2}\sigma_0\delta_c(1 + \lambda_2 - \lambda_1)$. These cohesive zone model parameters can be determined uniquely from the reactive MD simulations, detailed as follows: the fracture toughness is obtained via $\Gamma_c = G$, the maximum cohesive strength is obtained via $\sigma_0 = \sigma_P$, and the critical separation is determined via $\delta_c = d_c$. The shape parameters λ_1 and λ_2 satisfy the relation $1 + \lambda_2 - \lambda_1 = \frac{2G}{\sigma_p\delta_c}$, and they are determined by fitting the atomistic simulation curves, as shown in Figure 3(b). When the metal thin film of Ni changes to copper (Cu) or palladium (Pd), similar procedures will be used to perform reactive MD simulations and to determine parameters of CZM, as given in Figure A2. Table 1 summarizes these parameters that are determined from reactive MD simulations and will be input to FE models for macroscale FE analysis. For other different loading rates, similar procedures are also used to perform reactive MD simulations, as given in Figure A3, and to determine rate dependent CZM parameters. Table 2 summarizes the rate dependent interfacial

cohesive energy that is in good agreement with theoretical calculations based on Equation (11) and will be input in the FE analysis.

In FE simulations, the metal thin film was modeled by elastic-perfectly plasticity and the substrate SiO_2 was considered as an elastic material. The elastic parameters for substrate were Young's modulus E = 170 GPa and Poisson ration ν = 0.3 and for Ni film, E = 200 GPa, ν = 0.31, and yield stress σ_y = 400 MPa (Tanaka et al., 2010). In FE analysis, 2D plane strain model was employed to simulate the peeling experiments by using the ABAQUS/standard package. The length of thin film was 1 cm and the thickness varied from 300 nm to 2.4 um. The film and the substrate were meshed with 4-node bi-linear plane strain elements. At least four layers of elements were used along the thickness in the thin film to well capture the through-thickness stress distribution and bending deformation, which leads to 30000 to 250000 elements depending on film thickness. Mesh refinement with a high density was set near the interface of the metal layer, and mesh convergence was studied to confirm the discretization of model sufficiently enough for extracting converged steady-state peeling force. A displacement loading was applied to one end of the thin film when peeled from the bottom fixed substrate at a given peeling angle (α).

3.3 Experiments

The peeling process was performed in a custom-modified mechanical peeling apparatus equipped with a high-resolution force gauge (Mark-10; resolution, ±0.25%)(Wie et al., 2018). A thin layer of metal film with thickness ranging from 300 nm to 2.4 μm was prepared on a SOI wafer by using an e-beam evaporation (for thin film) or electroplating (for thick film). Three different metal film materials nickel (Ni), copper (Cu) and palladium (Pd) were investigated. The prepared specimen was firmly attached on a plastic Petri dish with a double-sided tape (Kapton), and then laminated by a commercial adhesive tape (3M) across the top surface. The Petri dish was mounted on the horizontal stage of the automatic peeling apparatus. DI water was poured to the Petri dish to completely immerse the film/substrate system to mimic a liquid environment. A well-defined peeling angle with a displacement rate was applied to the adhesive tape and to conduct the peeling experiments. During the experiments, the peeling

force and displacement were recorded. For comparison, the peeling experiments with the same settings in dry conditions without water in Petri dish were also performed.

4. Results

Figure 4 (a) shows the experimental measurement of peeling strength-displacement curves for Ni thin film with thickness of 300nm in both water and dry conditions at room temperature, where the peeling strength is the measured peeling force per unit width of film. The peeling angle was $\alpha = 90°$ and the peeling rate was $v_p = 6.7 \times 10^{-6}$m/s. The results show that the peeling strength increases at the beginning until a peak value reaches to where the interfacial debonding was initiated, and then gradually decreases till to eventual arrival of a stable stage. Besides, the stable-stage peeling strength is largely decreased in water condition (~0.6 J/m^2) in comparison with that in dry condition (~2.4 J/m^2), confirming that the presence of water molecules decreases the interfacial adhesion energy and promotes the interfacial debonding. In parallel, we performed FE simulations in both dry and water conditions, and also plot their peeling strength-displacement curves in Figure 4(a). Because all the materials parameters in FE models were determined from reactive MD simulations and are independent of experiments, the excellent agreement between FEA and experimental measurements validates our atomistic-continuum FE modeling, and FEA can also be used for practical predictions of the transfer printing of thin films in a liquid environment. **Figure 4 (b)** presents the strain distribution (ε) in Ni thin film near the interface debond tip. The results show that the maximum principal strain (ε_{max}) of Ni film in water condition is about 45% smaller than that in dry condition. The lower strain indicates that the liquid water environment could not only decrease the debonding energy of interface, but could also lead to reduction of mechanical deformation in thin film layer in the transfer process, thus benefiting mechanical integrity of the thin film-enabled devices. This decreased strain also demonstrates the synergistic and complex coupling effect between kinetic chemical reaction at interface and thin film peeling mechanics, consistent with theoretical analysis in Section 2.

When the thickness of Ni thin film increases, **Figure 5(a)** gives the further comparison of peeling strength–displacement responses between FE simulations and experimental results in

water condition, and the good agreement between them remains. Besides, the steady-state peeling strength is lower for a larger thickness, i.e. ~0.4 J/m^2 for the thickness of 1300 nm versus ~0.6 J/m^2 for the thickness of 300 nm. **Figure 5(b)** gives the variation of the steady-state peeling strength with thin film thickness from simulations and experiments in both dry and water conditions. Given the same thickness of films, the steady-state peeling strength is smaller in water environment than that in dry environment. More importantly, from Equations (22) and (24), with b=2 nm, $E_a{}^* = 39$k J/mol and N=1.6/m^2 (Vijayashankar et al., 2011), the steady-state peeling strength can be obtained in theory and is also plotted in Figure 5(b). These theoretical predictions are consistent with both FE simulations and experimental results in both dry and water environments. These experimental results, FE simulations and theoretical predictions further confirm the steady-state peeling strength decreases as the thin film thickness increases. It is expected that the peeling strength will converge to the interfacial adhesion energy when the film thickness is large enough, where the bending-induced plastic deformation in the film can be neglected and the peeling strength is mainly dominated by interface de-cohesion, which is consistent with Equation (21). As a consequence, the peeling strength is equal to the interfacial adhesion energy or interface debonding energy (Allendorf et al., 1995; Lane, 2003) and they are $G = 0.19$ J/m^2 in water condition and $G = 0.81$ J/m^2 in dry condition at a peeling rate $v_p = 6.7 \times 10^{-6}$ m/s, which agrees well with the theoretical analysis ($G = 0.22$J/m^2 and $G = 0.74$J/m^2 in water and dry condition, respectively) from Equations (22) and (24).

Figure 5(c) shows the FE simulations and experiment results of peeling strength–displacement responses at two different peeling rates in the water environment, $v_p = 2.5 \times 10^{-3}$m/s and $v_p = 6.7 \times 10^{-6}$m/s. The peeling angle was $\alpha = 90°$. The thickness of Ni thin film was taken 2400 nm and the contribution of plastic deformation in film can be neglected according to Figure 5(b). Note that when loading rates change, the CZM parameters in the FE simulations are determined from separate MD simulations, as shown in Figure A3 and Table 2. They are similar to those shown in Figure 4(a), with an initial increase of the peeling strength and then eventually arrival of a stable stage. The continuous good agreement between FE simulations and experiments indicates the atomistic-continuum FE analysis can capture the rate

dependent water environment-assisted peeling process. In addition, a higher peeling rate leads to a higher steady-state peeling strength, which also agrees with the theoretical analysis in Equation (11). **Figure 5(d)** shows the variation of the steady-state peeling strength with the peeling rate. It further confirms that the steady-state peeling strength of the film decreases as the peeling rate decreases. Similar to theoretical calculations in Figure 5 (b), the effect of peeling rate on the peeling strength can also be calculated in theory via Equations (22) and (24), and the results agree with both FE simulations and experiments in both dry and water conditions, as shown in **Figure 5 (d)**. When the peeling rate is sufficiently small, the steady-state peeling strength is constant in both in water and dry conditions. Besides, because the plastic deformation in the thin film with thickness $t = 2400$ nm can be neglected, the peeling behavior is dominated by the kinetic chemical reaction controlled interfacial delamination in both two conditions, and these approximately constant peeling strengths are equal to the intrinsic adhesion energy G_0 in their corresponding environments, as obtained in reactive MD simulations or theoretical calculations via Equation (24). We should note that in our current study, we focus on the effect of loading rate no more than 0.03 m/s, where the penetration rate of the liquid to the fracture front is higher than the propagation rate of the fracture front, i.e., the liquid is always present at the fracture tip. When the peeling rate is more than 0.03 m/s, the cavitation or/and bubble could occur at the debond tip (MICHALSKE and Frechette, 1980), leading to an incomplete contact between liquid and interfacial crack tip, and the chemomechanics model that takes into account the vapor pressure to the crack initiation and growth may be required (Vlassak et al., 2005).

Further, we performed peeling experiments and FE simulations in water condition by replacing Ni films with Cu and Pd. When Ni was replaced by either Cu or Pd, the computational settings and implementation procedures were the same except the ReaxFF parameters(Psofogiannakis et al., 2015; Senftle et al., 2016) in the reactive MD simulations and the CZM parameters were determined as listed in Table 1 and input FE models. Their elastoplastic parameters in FE simulations were E = 128GPa, ν = 0.36, and σ_y= 100 MPa for Cu; E = 121GPa, ν = 0.39, and σ_y= 220 MPa for Pd (Dolbow and Gosz, 1996). **Figure 5(e)** gives the comparison of peeling strength–displacement curves for Ni and Cu. The thin film

thickness of both materials was 300 nm. The peeling angle was $\alpha = 90°$ and the peeling rate was $v_p = 6.7 \times 10^{-6}$ m/s. A higher peeling strength is obtained for the Cu//SiO_2 that of Ni/SiO_2 interface, indicating a stronger adhesion strength for Cu/SiO_2 interface. **Figure 5(f)** shows the steady-state peeling strength as a function of film thickness for different thin film materials in water condition. Similar to that observation for Ni film in Figure 5(b), the steady-state peel strength of the film decreases as the thickness of the film increases for both Pd and Cu. Through Equations (22) and (24), where M is the Cu and Pd, respectively, their corresponding theoretical steady-state peeling strength can be calculated and shows good agreement with both FE simulations and experimental measurements, as shown in Figure 5(f). In particular, when the thickness of films is sufficiently large, and their plastic deformation can be neglected. Besides, because the peeling rate $v_p = 6.7 \times 10^{-6}$m/s is small enough, their interface debonding energy is equal to G_0 and can be obtained from experiments and FE simulations. They are $G_0 = 0.39$ J/m^2 for Cu/SiO_2 interface and $G_0 = 0.17$J/m^2 for Pd/SiO_2 interface in water condition, which agrees with theoretical calculations ($G_0 = 0.34$J/m^2 for Cu/SiO_2 interface and $G_0 = 0.19$ J/m^2 for Pd/SiO_2 interface), and reactive MD simulations ($G_0 = 0.36$J/m^2 for Cu/SiO_2 interface and $G_0 = 0.21$ J/m^2 for Pd/SiO_2 interface).

Figure 6 summarizes the intrinsic interface adhesion energy G_0 for metal (Ni, Cu and Pd) thin film on SiO_2 substrate in both dry and water environments, and all of them agree well among reactive MD simulations, theoretical calculations (Equations (23) and (24)) and experiments. Besides, our theoretical and reactive MD simulation results agree with experimental measurements on gold (Au) thin film on SiO_2 substrate system in both dry and wet environments (Vijayashankar et al., 2011), which further validates the robustness of our proposed chemomechanics theory in Section 2 and atomistic-continuum computational modeling in Section 3. In addition, the adhesion energy in water environment is smaller than that in dry environment, which indicates that the liquid-assisted transfer technique could be applied to a relative broad range of interfacial materials.

In addition, we have investigated the effect of the peeling angle on peeling strength. **Figure 7(a)** gives the FE simulations and experimental results of peeling strength–displacement responses of a Ni thin film under two peeling angles. The thin film thickness was $t = 300$ nm

and the peeling rate was $v_p = 2.5 \times 10^{-3}$ m/s. Similar to that in Figure 5, good agreement between FE simulations and experiments remains. Besides, the peeling strength becomes larger when the peeling angle is smaller. **Figure 7(b)** gives the effect of peeling angle on the steady-state peeling strength in water condition, further confirming that a smaller peeling strength at a lager peeling angle. More importantly, these FE simulations and experimental results are well captured by the theoretical predictions, which further validates the proposed chemomechanics theory.

5. Theoretical map of applications toward successful transfer of silicon membrane

In the practical applications of transferring a functional thin film from a substrate, in particular a fragile functional layer, the transfer will not only require a success of detachment of functional thin film from substrate, but will also not allow a severe deformation (e.g. no more than the failure limit) in the functional layer so as to keep its as-fabricated properties such as electric and thermal properties. Our proposed chemomechanics theory that takes into account both mechanical deformation of functional thin film and interfacial delamination could provide a guidance for systematically optimizing the transfer conditions including material selection, loading rate, and environment to achieve a successful transfer. As an application demonstration, we took a Si nanomembrane as a functional thin film that is often employed and designed for strain and temperature sensors deposited on the SOI wafer with nickel as a separation layer (Wie et al., 2018), referred to Figure 1. The thickness of Si nanomembrane and separation layer nickel was taken 100 nm and 600 nm, respectively. The Young's modulus and Poisson's ratio of Si membrane were 170 GPa and 0.3 in FE simulations, respectively, and the failure strain of silicon membrane was $\varepsilon_f = 1\%$ (Khang et al., 2006). Assume the mismatch between Si membrane and separation Ni layer will not affect the bending deformation, with Equation (21), the maximum strain ε_{max} in the Si membrane/separation layer during the steady-state peeling process can be obtained via $\sigma_y \varepsilon_{max} t - \frac{5{\sigma_y}^2 t}{2E} + \frac{5{\sigma_y}^3 t}{3E^2\ \varepsilon_{max}} = P(1 - cos\alpha) - G(\ v_p)$, and $\varepsilon_{max} = \frac{K_{max} t}{2}$. When $\varepsilon_{max} < \varepsilon_f$, the function layer will not be damaged and the transfer process is successful. In contrast, if $\varepsilon_{max} > \varepsilon_f$, the function layer will be damaged and the transfer is failed.

Figure 8(a) gives a theoretical map of competition between the maximum principle plane strain in Si nanomembrane/Ni separation layer when peeled in water condition and dry condition with different peeling velocities and angles. The theoretical map shows that the maximum strain in the Si nanomembrane increases with the increasing of peeling rate and decreasing of peeling angle. For a given peeling angle and rate, the maximum strain when peeled in water condition is smaller than that in dry condition. Based on the competition between ε_{max} and ε_f, we can identify that a larger peeling angle and smaller peeling rate will be favorable to a successful transfer of the Si nanomembrane in both water and dry conditions. In contrast, only water environment will lead to a success transfer at a smaller peeling angle and larger peeling rate. At a relatively large peeling rate but a very small peeling angle, peeling in both water and dry conditions will lead to $\varepsilon_{max} > \varepsilon_f$ which is not suggested for achieving a successful transfer. When the peeling rate is beyond a critical value (0.03 m/s here), an incomplete immerse of interfacial crack tip into liquid may happen due to the occurrence of bubbles and cavitation that are beyond our current theory, as we discussed in Section 2. As the separation nickel layer thickness (t) and material properties (σ_y/E) change, similar to Figure 8(a), a theoretical map can also be given, as shown in **Figure 8(b)**. Larger t and σ_y/E will lead to $\varepsilon_{max} > \varepsilon_f$ in both water and dry conditions, and as a consequence, the transfer will be successful. We will have $\varepsilon_{max} < \varepsilon_f$ in both water and dry conditions at a very small t and σ_y/E, leading to the fail of transfer; With a proper σ_y/E, we will have $\varepsilon_{max} > \varepsilon_f$ in dry condition but $\varepsilon_{max} < \varepsilon_f$ in water condition, indicating the water environment will be favorable to a successful transfer. **Figure 8(c)** shows FE results of principle plane strain distribution in the Si nanomembrane/nickel separation layer near the interface debond tip during peeling process in both water and dry conditions, where regions are depicted in black color when the strain exceeds ε_f. The comparison indicates that at a higher peeling rate ($v_p = 1 \times 10^{-3}$ m/s), peeling in dry condition will lead to damage and failure of Si nanomembrane, while not in water condition. With the further increasing of peeling rate ($v_p = 8 \times 10^{-3}$ m/s), the maximum strain ε_{max} in both dry and water conditions will exceed ε_f, leading to failure and damage of Si nanomembrane, consistent well with the theoretical map in Figure 8(a). Similar results can also be obtained when the peeling angle changes, and a proper peeling angle

is needed for a successful peeling in either dry or water condition, which is consistent with the theoretical analysis. With the same peeling loading, Figure 8(c) shows the strain in the water environment is always smaller than that in dry condition, which further indicates that the presence of liquid environment benefits the transfer of functional thin films.

6. Discussion

In our theoretical model of chemomechanics in Section 2, we predict the stead-state peeling strength via the energy conservation of the peeling process via $W_P = W_{ad} + W_d$, where the presence of liquid environment leads to the change of interfacial adhesion energy W_{ad} because of chemical reaction at the interface. In essence, the liquid molecules will not only lead to the chemical reaction between the interfacial chemical bonding, but will also interact with the solid materials through physical capillary force. Therefore, the change of the interfacial adhesion energy ΔW_{ad} due to the liquid environment should include both chemical contribution ${\Delta W_{ad}}^{che}$ and physical contribution ${\Delta W_{ad}}^{phy}$, i.e. $\Delta W_{ad} = {\Delta W_{ad}}^{che} + {\Delta W_{ad}}^{phy}$. For most interfacial materials that actively react with liquid, such as $M - O - Si$ in water, where M is Ni, Cu, Pd and Au, the change of interface adhesion energy due to the physical capillary interaction, ~10^{-3}-10^{-1} J/m^2 (Wang et al., 2009; Zhang et al., 2017b), is usually two orders of magnitude lower than that due to the chemical interaction, ~10^{0}-10^{1} J/m^2 (Kook and Dauskardt, 2002) and can be neglected, i.e. $\Delta W_{ad} = {\Delta W_{ad}}^{che}$, which is discussed in our theoretical analysis in Section 2. In some scenario of film/substrate system such as graphene/silicon system (Rafiee et al., 2012), where the presence of liquid media does not display any chemical reactivity with solid materials and only has physical vdW interactions with solid interfaces during transfer. As a consequence, we will have $\Delta W_{ad} = {\Delta W_{ad}}^{phy}$. The presence of liquid will modify the physical interaction via the capillary force and ${\Delta W_{ad}}^{phy}$ can be obtained with the help of the Young's equation by considering surface wetting properties of new fractured surfaces of thin film and substrate to liquid molecules (Zhang et al., 2017b). This capillary-mechanics can also be leveraged to promote the peeling of plastic films and inks (Wang et al., 2009; Zhang et al., 2017b) and graphene films (Ma et al., 2017; Zhang et al., 2017b).

7. Conclusion

In this work, we have developed a comprehensive chemomechanics theory for transfer printing of thin films in a liquid environment. In this theory, both kinetic chemical reaction of solid and liquid induced interfacial debonding and mechanical deformation of thin film are taken into account and coupled seamlessly to predict a rate dependent peeling force at the steady-state peeling process. The theoretical analysis shows that the presence of liquid medium will weaken the interfacial energy and promotes the interfacial debonding process with a lower peeling strength in comparison with that in dry conditions. We have further conducted reactive molecular dynamics simulations by using ReaxFF reactive force field, and the obtained intrinsic interfacial energy agrees well with theoretical predictions. The debonding information including intrinsic interfacial energy and traction-separation relation at the atomistic scale is integrated with cohesive zone model at the continuum scale and is implemented into the finite element (FE) model for multiscale simulations. An atomistic-continuum multiscale modeling framework is established for simulating the entire liquid-assisted peeling process. In parallel, the peeling experiments are performed on three different separation layer metal materials, Ni, Cu and Pd in both water and dry conditions under a series of peeling rate, peeling angles, and thickness of metals. The experimental measurements show excellent agreement with both theoretical predictions and FE analysis, and validate the proposed chemomechanics theory and established atomistic-continuum FE modeling. Besides, the FE analysis shows that the liquid-assisted transfer will lead to a lower stress/strain distribution in thin film and will benefit the enhancement of transfer yield of thin films with a reduced mechanical deformation. In addition, all analyses show that the peeling strength at the steady state decreases with the increasing of both thin film thickness and peeling angle, but increases with the increasing of peeling rate. Phase diagrams of transferring a Si nanomembrane are given to highlight the competition between mechanical deformation of functional thin films and the interfacial delamination during transfer process and to help optimize the peeling conditions of transferring of functional films in practical applications. Extended discussion on the effect of surface wettability on interfacial delamination due to the presence of liquid is also presented, and the analysis on its

competition with chemical reaction-induced driving force demonstrates their unique applications in transferring of different film/substrate system. The present study is expected to provide an immediate guidance for mechanical peeling and transferring of functional thin film materials from various growth substrates to target substrates to meet the needs in the fabrication of thin film enabled devices, where the liquid could be employed to tune the peeling strength and promote the interfacial delamination.

Acknowledgments: C.H.L. acknowledges the funding support from the Purdue University and partial support from the AFRL-S-114-054-002. B.X. acknowledges the funding support from the NSF-CMMI- 1728149 and the University of Virginia

Appendix A. Bending moment-curvature relation of thin film during peeling

In most flexible devices, the sacrificial thin film layer such as nickel, copper and gold is ductile materials and the elastic tension deformation during peeling experiment is very small and can be neglected(Kendall, 1975). Here we will focus on the bending deformation of thin film. **Figure A.1 (a)** illustrates the deformation configuration of thin film under a steady state peeling process, where the thin film with thickness t is peeled off from a flat rigid substrate by an external peeling strength P with a loading angle α, and P is defined as the peeling force per unit width. For a steady-state peeling, the thin film has a constant shape and it will not change with peeling time (Kim and Kim, 1988). Based on our previous work (Wie et al., 2018), the relationship between local bending moment and curvature can be calculated via $M(K) = -\int_{-\frac{t}{2}}^{\frac{t}{2}} \sigma\{\varepsilon\} \cdot y \cdot dy = -\int_{-\frac{t}{2}}^{\frac{t}{2}} \sigma\{-Ky\} \cdot y \cdot dy$, where y is the local coordinate in the tangent direction, and σ and ε are the local normal stress and strain, respectively. Consider an elastic-perfectly plastic constitutive relation for the bending deformation of thin film (Kim and Aravas, 1988; Wei, 2004), as illustrated in **Figure A.1 (b)**, and define, E and σ_y are the Young's modulus and yield stress of the thin film, respectively, at $0 \leq K \leq \frac{2\sigma_y}{Et}$, the local thin film at OA section is in elastic deformation and the bending moment is

$$M_1(K) = -\int_{-\frac{t}{2}}^{\frac{t}{2}} E(-Ky)ydy \tag{A.1}$$

At $\frac{2\sigma_y}{Et} < K < K_{max}$, the plastic deformation will happen at AB section of film, where K_{max} is the maximum curvature in the thin film. As a consequence, the corresponding bending moment is

$$M_2(K) = -\int_{-\frac{t}{2}}^{-\frac{\sigma_y}{EK}} \sigma_y ydy - \int_{-\frac{\sigma_y}{EK}}^{\frac{\sigma_y}{EK}} E(-Ky)ydy - \int_{\frac{\sigma_y}{EK}}^{\frac{t}{2}} \sigma_y ydy \tag{A.2}$$

Beyond K_{max}, the unloading elastic deformation in the peeled films will happen, and at $K_{max} - \frac{4\sigma_y}{Et} \leq K \leq K_{max}$, the bending moment at BC section of thin film can be calculated as

$$M_3(K) = -\int_{-\frac{t}{2}}^{-\frac{\sigma_y}{EK_{max}}}[\sigma_y - E(-K_{max}y + Ky)]ydy - \int_{-\frac{\sigma_y}{EK_{max}}}^{\frac{\sigma_y}{EK_{max}}} E(-Ky)ydy - \int_{\frac{\sigma_y}{EK_{max}}}^{\frac{t}{2}}[\sigma_y - E(-K_{max}y + Ky)]ydy \quad \text{(A.3)}$$

Further, at $0 \leq K \leq K_{max} - \frac{4\sigma_y}{ET}$, the moment of reverse plastic bending at CD section of thin film can be calculated as

$$M_4(K) = -\int_{-\frac{\sigma_y}{EK_{max}}}^{\frac{\sigma_y}{EK_{max}}} E(-Ky)ydy - 2\int_{-\frac{2\sigma_y}{E(K_{max}-K)}}^{-\frac{\sigma_y}{EK_{max}}}[\sigma_y - E(-K_{max}y + Ky)]ydy - 2\int_{-\frac{t}{2}}^{-\frac{2\sigma_y}{E(K_{max}-K)}}\sigma_y ydy \quad \text{(A.4)}$$

Reference:

Afferrante, L., Carbone, G., 2016. The ultratough peeling of elastic tapes from viscoelastic substrates. Journal of the Mechanics and Physics of Solids 96, 223-234.

Allendorf, M.D., Melius, C.F., Ho, P., Zachariah, M.R., 1995. Theoretical study of the thermochemistry of molecules in the Si-OH system. The Journal of Physical Chemistry 99, 15285-15293.

Bae, S., Kim, H., Lee, Y., Xu, X., Park, J.-S., Zheng, Y., Balakrishnan, J., Lei, T., Kim, H.R., Song, Y.I., 2010. Roll-to-roll production of 30-inch graphene films for transparent electrodes. Nature Nanotechnology 5, 574-578.

Begley, M.R., Collino, R.R., Israelachvili, J.N., McMeeking, R.M., 2013. Peeling of a tape with large deformations and frictional sliding. Journal of the Mechanics and Physics of Solids 61, 1265-1279.

Carlson, A., Bowen, A.M., Huang, Y., Nuzzo, R.G., Rogers, J.A., 2012. Transfer Printing Techniques for Materials Assembly and Micro/Nanodevice Fabrication. Advanced Materials 24, 5284-5318.

Carlson, A., Kim-Lee, H.-J., Wu, J., Elvikis, P., Cheng, H., Kovalsky, A., Elgan, S., Yu, Q., Ferreira, P.M., Huang, Y., 2011. Shear-enhanced adhesiveless transfer printing for use in deterministic materials assembly. Applied Physics Letters 98, 264104.

Chen, H., Feng, X., Huang, Y., Huang, Y., Rogers, J.A., 2013. Experiments and viscoelastic analysis of peel test with patterned strips for applications to transfer printing. Journal of the Mechanics and Physics of Solids 61, 1737-1752.

Cheng, H., Wu, J., Yu, Q., Kim-Lee, H.-J., Carlson, A., Turner, K.T., Hwang, K.-C., Huang, Y., Rogers, J.A., 2012. An analytical model for shear-enhanced adhesiveless transfer printing. Mechanics Research Communications 43, 46-49.

Cook, R.F., Liniger, E.G., 1993. Kinetics of indentation cracking in glass. Journal of the American Ceramic Society 76, 1096-1105.

Dolbow, J., Gosz, M., 1996. Effect of out-of-plane properties of a polyimide film on the stress fields in microelectronic structures. Mechanics of Materials 23, 311-321.

Fan, Z., Ho, J.C., Jacobson, Z.A., Razavi, H., Javey, A., 2008. Large-scale, heterogeneous integration of nanowire arrays for image sensor circuitry. Proceedings of the National Academy of Sciences 105, 11066-11070.

Fogarty, J.C., Aktulga, H.M., Grama, A.Y., Van Duin, A.C., Pandit, S.A., 2010. A reactive molecular dynamics simulation of the silica-water interface. The Journal of Chemical Physics 132, 174704.

Gao, Y., Zhou, M., 2013. Coupled mechano-diffusional driving forces for fracture in electrode materials. Journal of Power Sources 230, 176-193.

Hwang, S.W., Song, J.K., Huang, X., Cheng, H., Kang, S.K., Kim, B.H., Kim, J.H., Yu, S., Huang, Y., Rogers, J.A., 2014. High - Performance Biodegradable/Transient Electronics on Biodegradable Polymers. Advanced Materials 26, 3905-3911.

Jung, I., Shin, G., Malyarchuk, V., Ha, J.S., Rogers, J.A., 2010. Paraboloid electronic eye cameras using deformable arrays of photodetectors in hexagonal mesh layouts. Applied Physics Letters 96, 021110.

Kendall, K., 1975. Thin-film peeling-the elastic term. Journal of Physics D: Applied Physics 8, 1449.

Khang, D.-Y., Jiang, H., Huang, Y., Rogers, J.A., 2006. A stretchable form of single-crystal silicon for high-performance electronics on rubber substrates. Science 311, 208-212.
Kim, K.-S., Aravas, N., 1988. Elastoplastic analysis of the peel test. International Journal of Solids and Structures 24, 417-435.
Kim, K.-S., Kim, J., 1988. Elasto-plastic analysis of the peel test for thin film adhesion. Journal of Engineering Materials and Technology 110, 266-273.
Kinloch, A., Lau, C., Williams, J., 1994. The peeling of flexible laminates. International Journal of Fracture 66, 45-70.
Kook, S.-Y., Dauskardt, R.H., 2002. Moisture-assisted subcritical debonding of a polymer/metal interface. Journal of Applied Physics 91, 1293-1303.
Lane, M., 2003. Interface Fracture. Annual Review of Materials Research 33, 29-54.
Lawn, B., 1975. An atomistic model of kinetic crack growth in brittle solids. Journal of Materials Science 10, 469-480.
Lee, C.H., Kim, J.H., Zou, C., Cho, I.S., Weisse, J.M., Nemeth, W., Wang, Q., van Duin, A.C., Kim, T.S., Zheng, X., 2013. Peel-and-stick: mechanism study for efficient fabrication of flexible/transparent thin-film electronics. Scientific Reports 3, 2917.
Li, X., Zhu, Y., Cai, W., Borysiak, M., Han, B., Chen, D., Piner, R.D., Colombo, L., Ruoff, R.S., 2009. Transfer of large-area graphene films for high-performance transparent conductive electrodes. Nano Letters 9, 4359-4363.
Ma, D., Shi, J., Ji, Q., Chen, K., Yin, J., Lin, Y., Zhang, Y., Liu, M., Feng, Q., Song, X., 2015. A universal etching-free transfer of MoS2 films for applications in photodetectors. Nano Research 8, 3662-3672.
Ma, X., Liu, Q., Xu, D., Zhu, Y., Kim, S., Cui, Y., Zhong, L., Liu, M., 2017. Capillary-force-assisted clean-stamp transfer of two-dimensional materials. Nano Letters 17, 6961-6967.
Mahenderkar, N.K., Chen, Q., Liu, Y.-C., Duchild, A.R., Hofheins, S., Chason, E., Switzer, J.A., 2017. Epitaxial lift-off of electrodeposited single-crystal gold foils for flexible electronics. Science 355, 1203-1206.
Meitl, M.A., Zhu, Z.-T., Kumar, V., Lee, K.J., Feng, X., Huang, Y.Y., Adesida, I., Nuzzo, R.G., Rogers, J.A., 2005. Transfer printing by kinetic control of adhesion to an elastomeric stamp. Nature Materials 5, 33-38.
MICHALSKE, T.A., Frechette, V., 1980. Dynamic effects of liquids on crack growth leading to catastrophic failure in glass. Journal of the American Ceramic Society 63, 603-609.
Mueller, J.E., van Duin, A.C., Goddard III, W.A., 2010. Development and validation of ReaxFF reactive force field for hydrocarbon chemistry catalyzed by nickel. The Journal of Physical Chemistry C 114, 4939-4949.
Nam, S., Jiang, X., Xiong, Q., Ham, D., Lieber, C.M., 2009. Vertically integrated, three-dimensional nanowire complementary metal-oxide-semiconductor circuits. Proceedings of the National Academy of Sciences 106, 21035-21038.
Peng, Z., Chen, S., 2015. Effect of bending stiffness on the peeling behavior of an elastic thin film on a rigid substrate. Physical Review E 91, 042401.
Peng, Z., Wang, C., Chen, L., Chen, S., 2014. Peeling behavior of a viscoelastic thin-film on a rigid substrate. International Journal of Solids and Structures 51, 4596-4603.
Pirkle, A., Chan, J., Venugopal, A., Hinojos, D., Magnuson, C., McDonnell, S., Colombo, L., Vogel, E., Ruoff, R., Wallace, R., 2011. The effect of chemical residues on the physical and

electrical properties of chemical vapor deposited graphene transferred to SiO2. Applied Physics Letters 99, 122108.
Plimpton, S., 1995. Fast parallel algorithms for short-range molecular dynamics. Journal of Computational Physics 117, 1-19.
Psofogiannakis, G.M., McCleerey, J.F., Jaramillo, E., Van Duin, A.C., 2015. ReaxFF reactive molecular dynamics simulation of the hydration of Cu-SSZ-13 zeolite and the formation of Cu dimers. The Journal of Physical Chemistry C 119, 6678-6686.
Qian, J., Lin, J., Xu, G.-K., Lin, Y., Gao, H., 2017. Thermally assisted peeling of an elastic strip in adhesion with a substrate via molecular bonds. Journal of the Mechanics and Physics of Solids 101, 197-208.
Rafiee, J., Mi, X., Gullapalli, H., Thomas, A.V., Yavari, F., Shi, Y., Ajayan, P.M., Koratkar, N.A., 2012. Wetting transparency of graphene. Nature Materials 11, 217.
Regan, W., Alem, N., Alemán, B., Geng, B., Girit, Ç., Maserati, L., Wang, F., Crommie, M., Zettl, A., 2010. A direct transfer of layer-area graphene. Applied Physics Letters 96, 113102.
Senftle, T.P., Van Duin, A.C., Janik, M.J., 2016. Methane activation at the Pd/CeO2 interface. ACS Catalysis 7, 327-332.
Suk, J.W., Kitt, A., Magnuson, C.W., Hao, Y., Ahmed, S., An, J., Swan, A.K., Goldberg, B.B., Ruoff, R.S., 2011. Transfer of CVD-grown monolayer graphene onto arbitrary substrates. ACS Nano 5, 6916-6924.
Tanaka, K., Isokawa, Y., Asano, H., Kimachi, H., 2010. Fatigue properties of nano-crystalline nickel electrodeposited thin films. Journal of the Society of Materials Science, Japan 59, 315-321.
Tvergaard, V., Hutchinson, J.W., 1993. The influence of plasticity on mixed mode interface toughness. Journal of the Mechanics and Physics of Solids 41, 1119-1135.
Van Duin, A.C., Dasgupta, S., Lorant, F., Goddard, W.A., 2001. ReaxFF: a reactive force field for hydrocarbons. The Journal of Physical Chemistry A 105, 9396-9409.
Vijayashankar, D., Zhu, H., Garg, S., Teki, R., Ramprasad, R., Lane, M.W., Ramanath, G., 2011. Atomistic mechanisms of moisture-induced fracture at copper-silica interfaces. Applied Physics Letters 99, 133103.
Vlassak, J.J., Lin, Y., Tsui, T.Y., 2005. Fracture of organosilicate glass thin films: environmental effects. Materials Science and Engineering: A 391, 159-174.
Wang, J., Qian, J., Gao, H., 2009. Effects of capillary condensation in adhesion between rough surfaces. Langmuir 25, 11727-11731.
Wei, Y., 2004. Modeling nonlinear peeling of ductile thin films—critical assessment of analytical bending models using FE simulations. International Journal of Solids and Structures 41, 5087-5104.
Wei, Y., Hutchinson, J.W., 1997. Nonlinear delamination mechanics for thin films. Journal of the Mechanics and Physics of Solids 45, 1137-1159.
Wie, D.S., Zhang, Y., Kim, M.K., Kim, B., Park, S., Kim, Y.-J., Irazoqui, P.P., Zheng, X., Xu, B., Lee, C.H., 2018. Wafer-recyclable, environment-friendly transfer printing for large-scale thin-film nanoelectronics. Proceedings of the National Academy of Sciences, 201806640.
Wiederhorn, S., Fuller, E.R., Thomson, R., 1980. Micromechanisms of crack growth in ceramics and glasses in corrosive environments. Metal Science 14, 450-458.
Xia, S., Ponson, L., Ravichandran, G., Bhattacharya, K., 2013. Adhesion of heterogeneous thin

films—I: Elastic heterogeneity. Journal of the Mechanics and Physics of Solids 61, 838-851.
Xu, B., Akhtar, A., Liu, Y., Chen, H., Yeo, W.H., Park, S.I., Boyce, B., Kim, H., Yu, J., Lai, H.Y., 2016. An epidermal stimulation and sensing platform for sensorimotor prosthetic control, management of lower back exertion, and electrical muscle activation. Advanced Materials 28, 4462-4471.
Xu, R., Zhao, K., 2018. Corrosive fracture of electrodes in Li-ion batteries. Journal of the Mechanics and Physics of Solids 121, 258-280.
Xue, Y., Zhang, Y., Feng, X., Kim, S., Rogers, J.A., Huang, Y., 2015. A theoretical model of reversible adhesion in shape memory surface relief structures and its application in transfer printing. Journal of the Mechanics and Physics of Solids 77, 27-42.
Yao, H., Della Rocca, G., Guduru, P., Gao, H., 2008. Adhesion and sliding response of a biologically inspired fibrillar surface: experimental observations. Journal of The Royal Society Interface 5, 723-733.
Yoon, J., Jo, S., Chun, I., Jung, I., Kim, H., Meitl, M., Menard, E., Li, X., Coleman, J., Paik, U., Rogers, J., 2010. GaAs photovoltaics and optoelectronics using releasable multilayer epitaxial assemblies. Nature 465, 329-U380.
Yoon, J., Lee, S.M., Kang, D., Meitl, M.A., Bower, C.A., Rogers, J.A., 2015. Heterogeneously integrated optoelectronic devices enabled by micro - transfer printing. Advanced Optical Materials 3, 1313-1335.
Zhang, M., Qu, J., Rice, J.R., 2017a. Path independent integrals in equilibrium electro-chemo-elasticity. Journal of the Mechanics and Physics of Solids 107, 525-541.
Zhang, Y., Liu, Q., Xu, B., 2017b. Liquid-assisted, etching-free, mechanical peeling of 2D materials. Extreme Mechanics Letters 16, 33-40.
Zhao, H., Wei, Y., 2008. Inverse analysis determining interfacial properties between metal film and ceramic substrate with an adhesive layer. Acta Mechanica Sinica 24, 297-303.

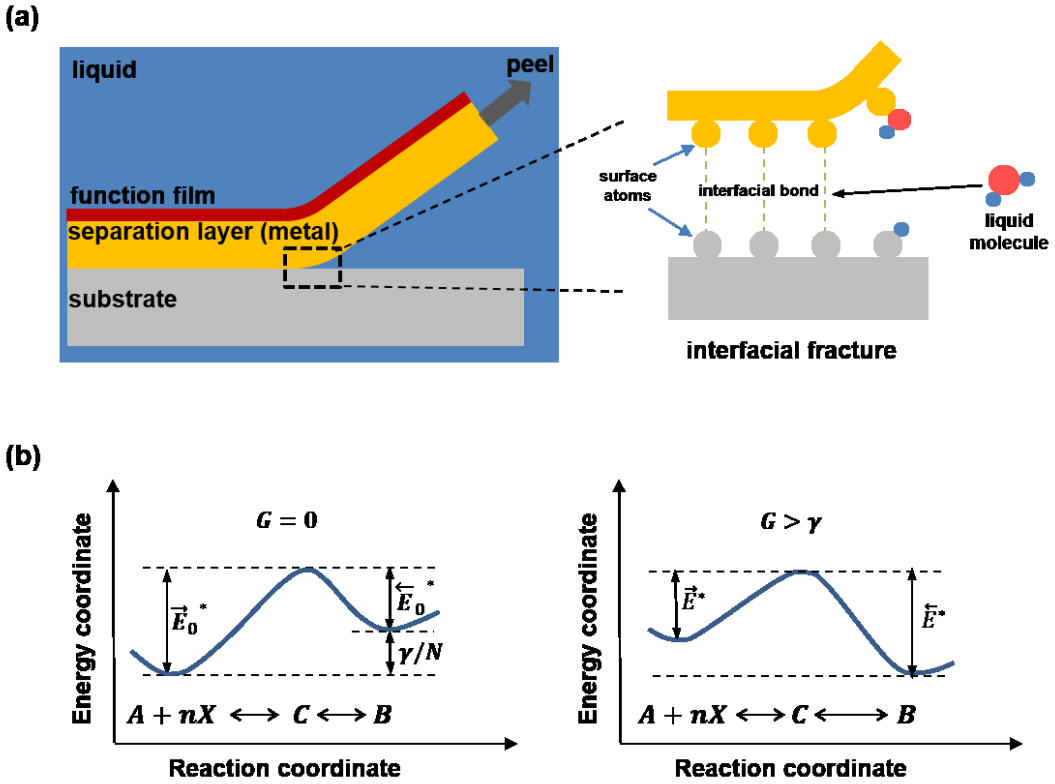

Figure 1. Peeling mechanics model for the transfer of a functional film in a liquid environment and energy landscape. (a) Schematic illustration of peeling a functional film from a substrate with a separation layer between them (left) and of atomistic debonding at interface between separation layer and substrate (right) in a liquid environment. **(b)** Energy diagram for interfacial bond rupture and healing by chemical reaction without (left) and with (right) mechanical loading. The chemical reaction follows $A + nX \leftrightarrow C \leftrightarrow B$. G is external mechanical energy, γ is surface energy per unit area and N is the number of interfacial bond per unit area. $\vec{E}_0^{\,*}$ and $\overleftarrow{E}_0^{\,*}$ are the energy barrier for interfacial bonding rupture and healing with respect to a transition state without mechanical loading, respectively; $\vec{E}^*$ and $\overleftarrow{E}^*$ are the energy barrier for interfacial bonding rupture and healing with mechanical loading, respectively and $G > \gamma$.

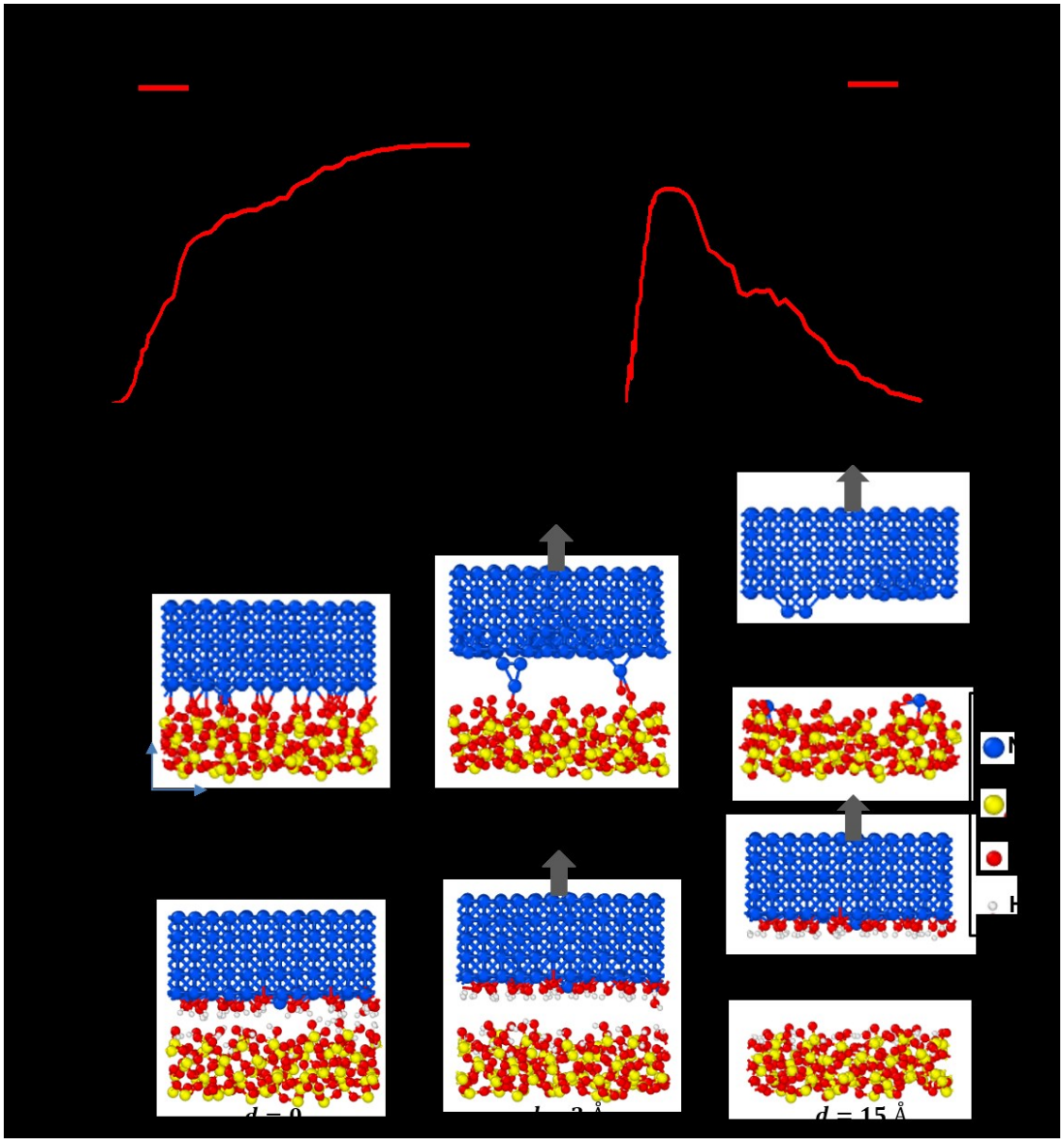

Figure 2. Reactive molecular dynamics (MD) simulations on the separation of interface in the nickel (Ni) thin film and SiO_2 substrate system in both water and dry conditions. (a) Variation of the system potential energy and **(b)** Interfacial traction stress with separation distance in both dry and water conditions. **(c)** MD simulation snapshots at different separation distances in both dry and water conditions.

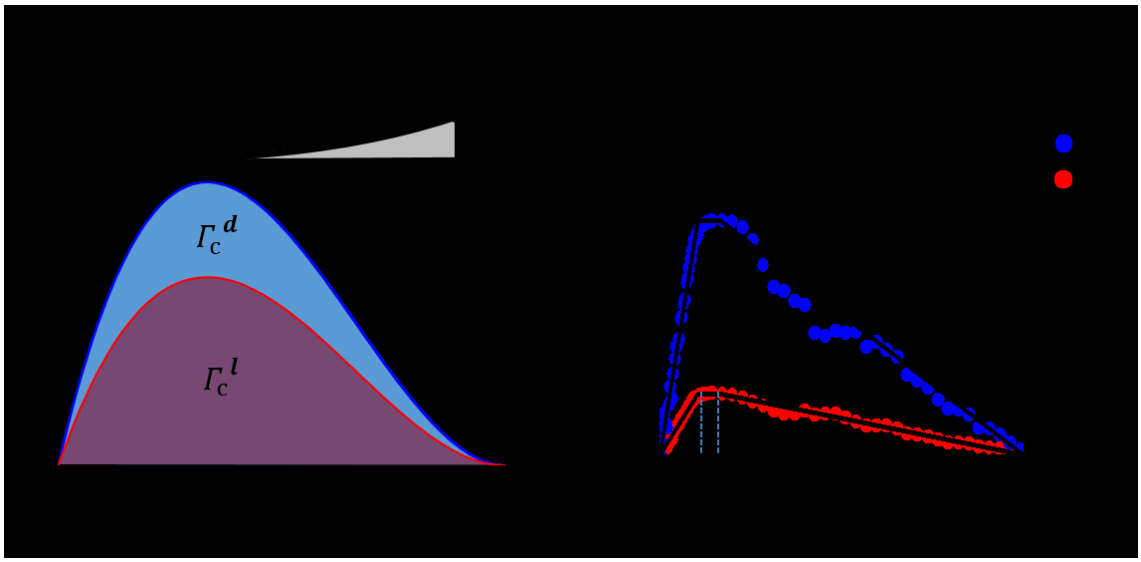

Figure 3. **Cohesive zone model (CZM) for continuum-scale finite element analysis that could be integrated with reactive MD simulations**. **(a)** Schematic illustration of the constitute traction – separation law of the cohesive zone model. Γ_c^d and Γ_c^l are the enclosed area of traction – separation curves and represent the fracture toughness in dry and liquid environment, respectively. **(b)** Trapezium shaped traction-separation relation that can fit MD simulation data well for nickel (Ni) material in both dry and water conditions.

Table 1. Parameters of cohesive zone model (CZM) that are obtained from reactive MD simulations and used for FE analysis

Material	**Condition**	Γ_c **(J/m²)**	σ_0 **(GPa)**	δ_c **(nm)**	λ_1, λ_2
Ni	dry	0.77	0.90	1.61	0.11, 0.17
Ni	water	0.20	0.23	1.60	0.10, 0.16
Cu	dry	0.82	0.96	1.61	0.11, 0.17
Cu	water	0.34	0.40	1.60	0.10, 0.16
Pd	dry	0.61	0.71	1.63	0.12, 0.18
Pd	water	0.21	0.24	1.62	0.11, 0.17

Table 2. Rate dependent interfacial cohesive energy Γ_c of Ni film that are obtained from reactive MD simulations with different loading rates and used for FE analysis. Theoretical calculations (Equation (11)) are also given for comparison.

Loading rate (m/s)	Γ_c (J/m^2) (dry)		Γ_c (J/m^2) (water)	
	MD	Theory	MD	Theory
6.7×10^{-6}	0.78	0.75	0.21	0.22
1.7×10^{-4}	1.03	0.96	0.27	0.25
2.5×10^{-3}	1.41	1.33	0.54	0.49

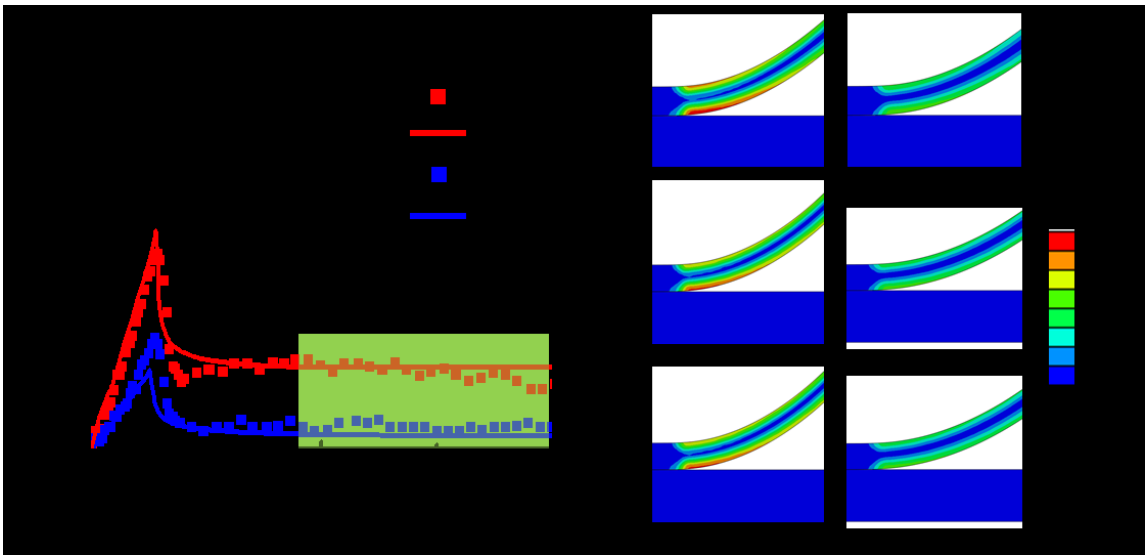

Figure 4. Comparison of peeling experiments on the nickel (Ni) film-SiO_2 substrate and finite element analysis (FEA) in dry and water conditions. (a) Experimental measurement and FEA of peeling strength - displacement responses of nickel (Ni) thin film from SiO_2 substrate in dry and water conditions. **(b)** Principal strain distributions of FEA in the thin film near the debond tip during peeling process in water and dry conditions.

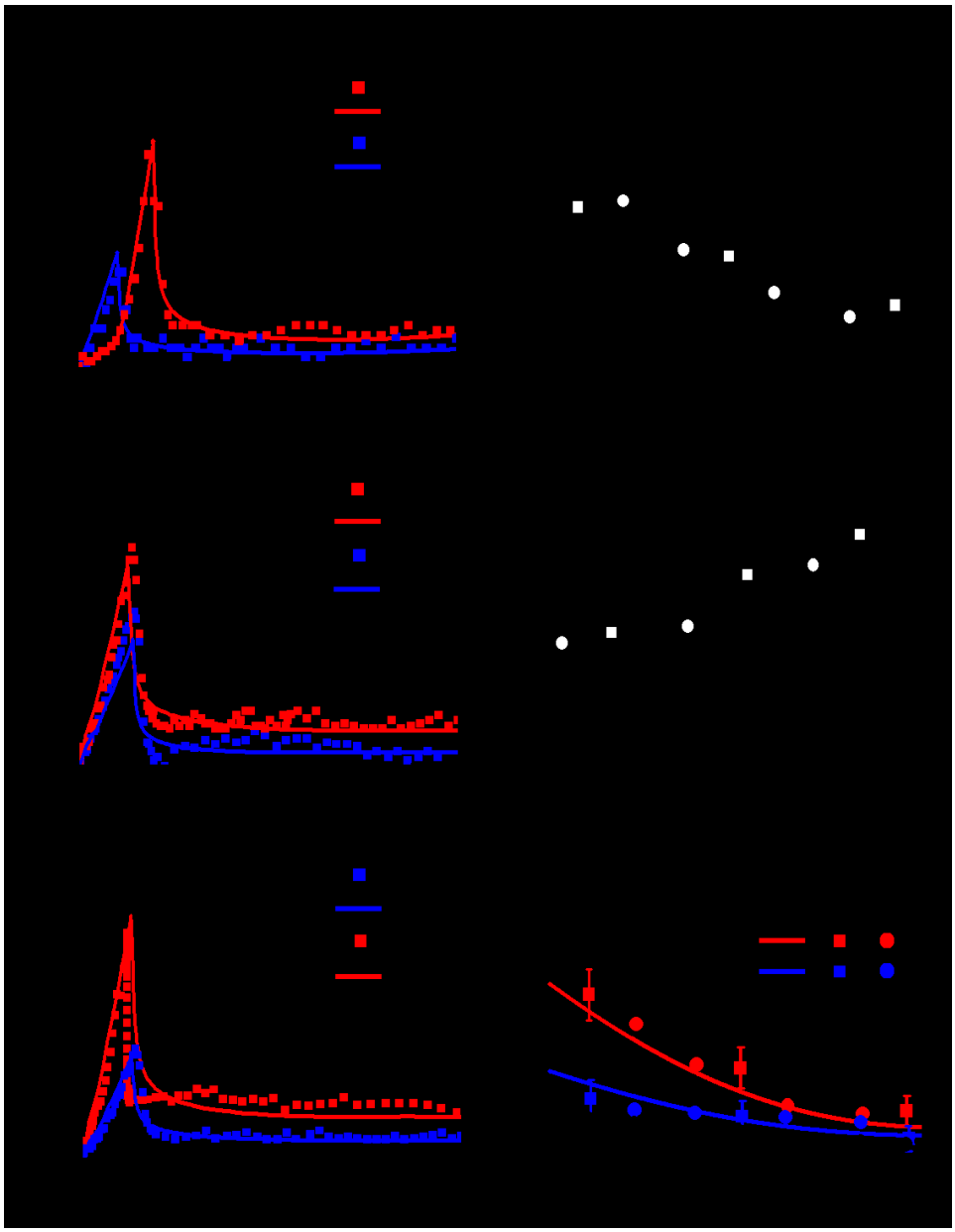

Figure 5. Comparison of peeling of thin films from SiO_2 substrate among experiments, finite element analysis (FEA), and theoretical predictions in a water environment. (a) Experimental measurements and FEA of peeling strength-displacement responses of nickel (Ni) thin film with different thicknesses. **(b)** Comparison of the steady-state peeling strength of nickel (Ni) thin film with different thicknesses among experiments, FEA and theoretical calculations in both dry and water environments. **(c)** Experimental measurements and FEA of peeling strength-displacement responses of nickel (Ni) thin film in water condition under different peeling rates. **(d)** Comparison of the steady-state peeling strength of nickel (Ni) thin film among experiments, FEA and theoretical calculations in both dry and water environments under different peeling rates. **(e)** Experimental measurements and FEA of peeling strength-displacement responses of nickel (Ni) and copper (Cu) thin films in water condition. **(f)** Comparison of the steady-state peeling strength of nickel (Ni), copper (Cu) and palladium (Pd) thin film among experiments, FEA and theoretical calculations in both dry and water environments with different thin film thickness.

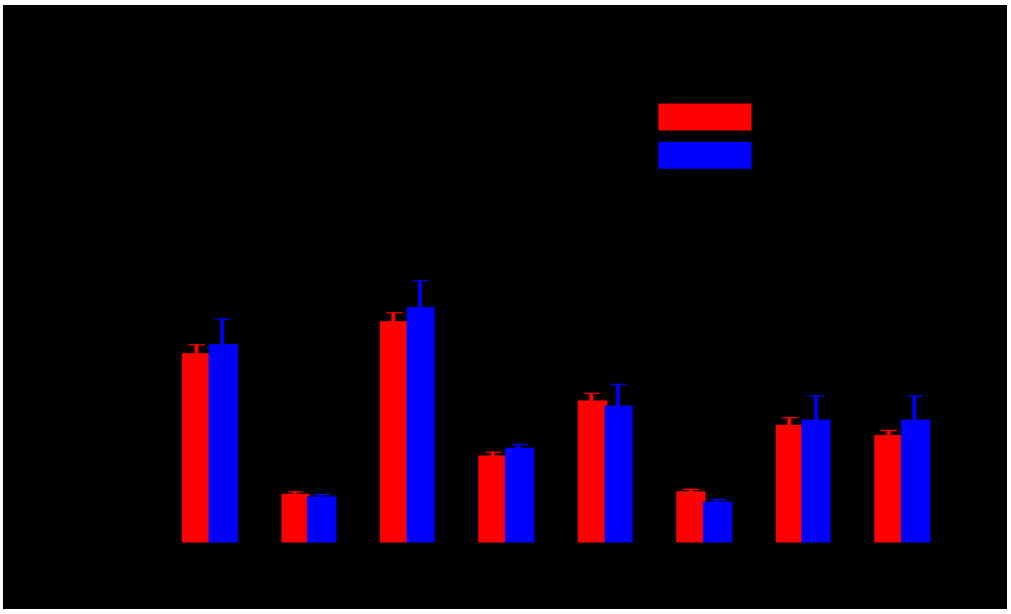

Figure 6. Comparison of intrinsic interfacial adhesion energy (G_0) of different metal separation layer from SiO_2 substrate among theoretical calculations (Equations (23) and (24)), experimental measurements and reactive MD simulations in both water and dry environments.

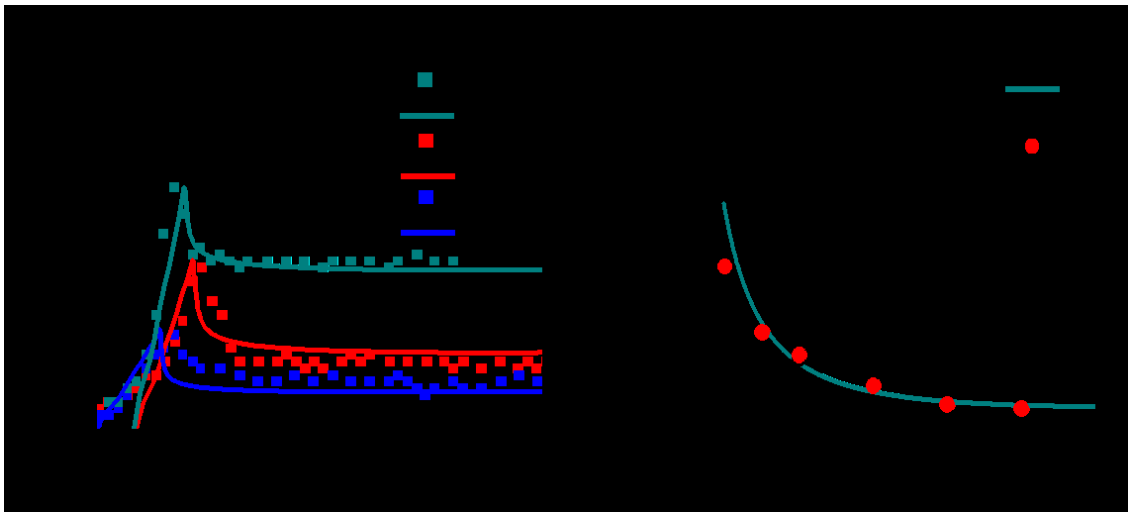

Figure 7. Effect of peeling angle on peeling of nickel (Ni) thin films from SiO_2 substrate in water environments. (a) Experimental measurements and FEA of peeling strength-displacement response of nickel (Ni) thin film in water condition under different peeling angles. **(b)** Comparison of the steady-state peeling strength of nickel (Ni) thin film among experiments, FEA and theoretical calculations in water environments under different peeling angles.

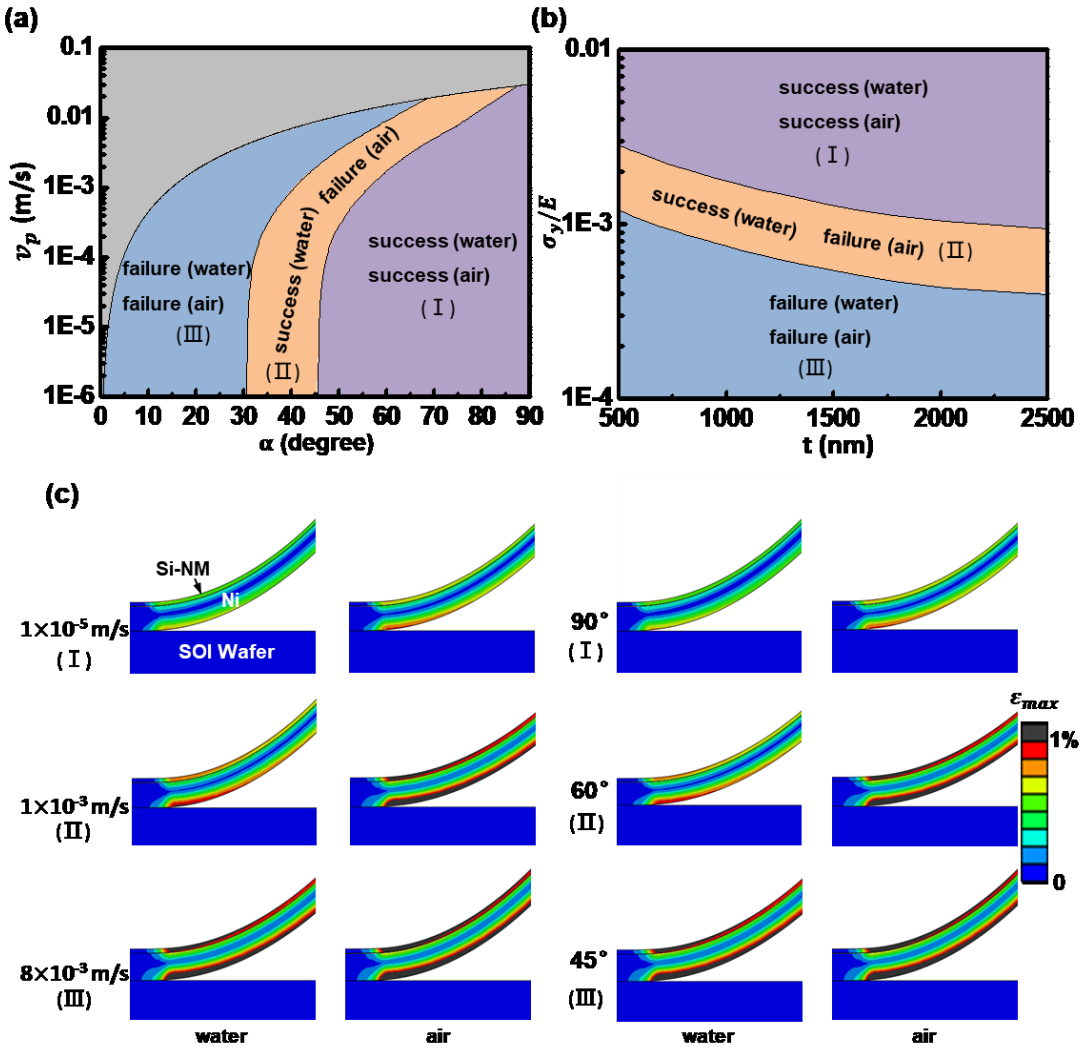

Figure 8. Application demonstrations of chemomechanics theory for transferring silicon nanomembrane (Si-NM) in dry and water environment. Theoretical phase diagram for transferring silicon membrane under **(a)** different loading conditions and **(b)** materials parameters. **(c)** Plane strain distribution of silicon membrane/nickel (Ni) separation layer under representative peeling conditions. The failure strain 1% of silicon membrane is used as a standard in the plots and contours for determining success (maximum strain <1%) and failure (maximum strain >1%), and the failure region is set black in color in strain contours.

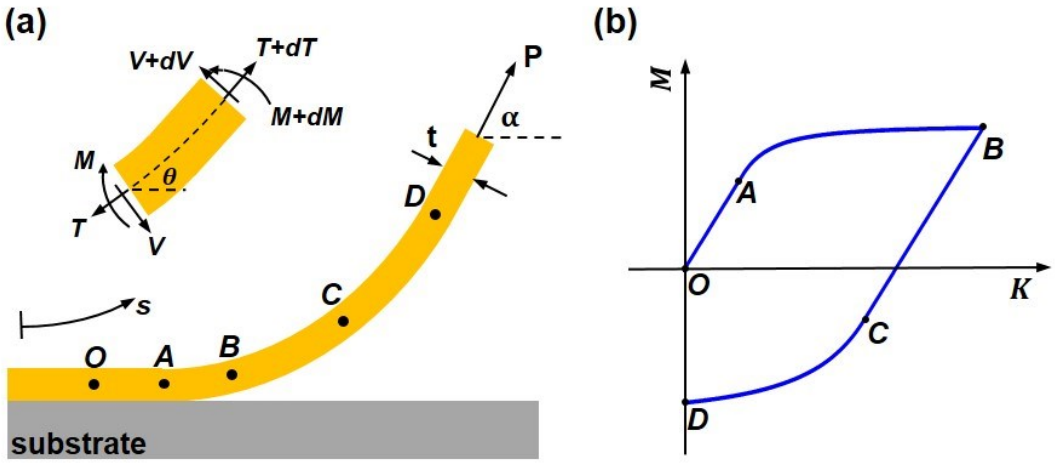

Figure A1. Mechanical deformation model of peeling a thin film from substrate. (a) Schematics of the configuration of thin film with mechanical bending deformation during a steady-state peeling process. A peeling force P is applied to the separation layer with a loading angle α, and the inset highlights the bending deformation of a unit length. **(b)** Bending moment – curvature relation of the thin film and its corresponding mechanical deformation behavior at each stage in (a).

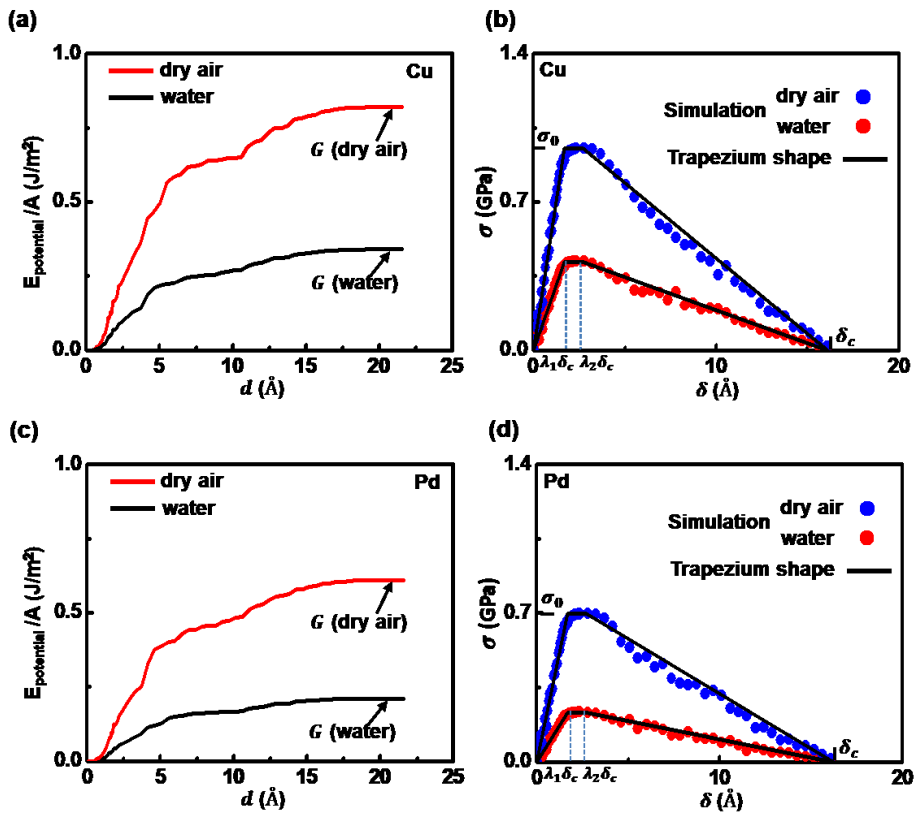

Figure A2. (a) Variation of the system potential energy and **(b)** Interfacial traction stress with separation distance in both dry and water conditions for material of thin film copper (Cu). **(c)** Variation of the system potential energy and **(d)** Interfacial traction stress with separation distance in both dry and water conditions for material of thin film palladium (Pd).

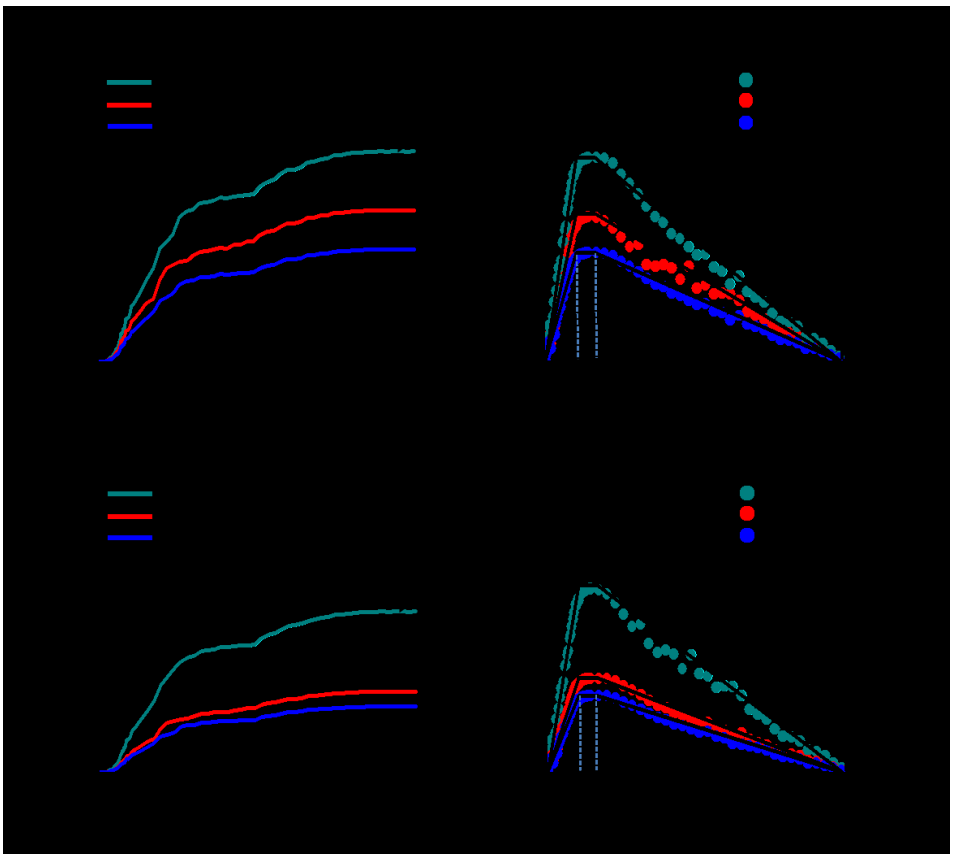

Figure A3. (a) Variation of the system potential energy and **(b)** Interfacial traction stress with separation distance for Ni thin film in dry condition at different loading rates. **(c)** Variation of the system potential energy and **(d)** Interfacial traction stress with separation distance for Ni thin film in water condition at different loading rates.